

Article

Viscoelastic MHD Nanofluid Thin Film Flow over an Unsteady Vertical Stretching Sheet with Entropy Generation

Asad Ullah ^{1,2} , Zahir Shah ¹ , Poom Kumam ^{3,4,5,*} , Muhammad Ayaz ¹, Saeed Islam ¹  and Muhammad Jameel ¹

¹ Department of Mathematics, Abdul Wali Khan University, Mardan 23200, Khyber Pakhtunkhwa, Pakistan; asad.ullah@kust.edu.pk (A.U.); Zahir1987@yahoo.com (Z.S.); mayazmath@awkum.edu.pk (M.A.); saeedislam@awkum.edu.pk (S.I.); muhammadjameel198@gmail.com (M.J.)

² Institute of Numerical Sciences, Kohat University of Science & Technology, Kohat 26000, Khyber Pakhtunkhwa, Pakistan

³ KMUTT-Fixed Point Research Laboratory, Room SCL 802 Fixed Point Laboratory, Science Laboratory Building, Department of Mathematics, Faculty of Science, King Mongkut's University of Technology Thonburi (KMUTT), 126 Pracha-Uthit Road, Bang Mod, Thrung Khru, Bangkok 10140, Thailand

⁴ KMUTT-Fixed Point Theory and Applications Research Group, Theoretical and Computational Science Center (TaCS), Science Laboratory Building, Faculty of Science, King Mongkut's University of Technology Thonburi (KMUTT), 126 Pracha-Uthit Road, Bang Mod, Thrung Khru, Bangkok 10140, Thailand

⁵ Department of Medical Research, China Medical University Hospital, China Medical University, Taichung 40402, Taiwan

* Correspondence: poom.kum@kmutt.ac.th; Tel.: +66-2-4708-994

Received: 3 April 2019; Accepted: 28 April 2019; Published: 6 May 2019



Abstract: The boundary-layer equations for mass and heat energy transfer with entropy generation are analyzed for the two-dimensional viscoelastic second-grade nanofluid thin film flow in the presence of a uniform magnetic field (MHD) over a vertical stretching sheet. Different factors, such as the thermophoresis effect, Brownian motion, and concentration gradients, are considered in the nanofluid model. The basic time-dependent equations of the nanofluid flow are modeled and transformed to the ordinary differential equations system by using similarity variables. Then the reduced system of equations is treated with the Homotopy Analysis Method to achieve the desire goal. The convergence of the method is prescribed by a numerical survey. The results obtained are more efficient than the available results for the boundary-layer equations, which is the beauty of the Homotopy Analysis Method, and shows the consistency, reliability, and accuracy of our obtained results. The effects of various parameters, such as Nusselt number, skin friction, and Sherwood number, on nanofluid film flow are examined. Tables are displayed for skin friction, Sherwood number, and Nusselt number, which analyze the sheet surface in interaction with the nanofluid flow and other informative characteristics regarding this flow of the nanofluids. The behavior of the local Nusselt number and the entropy generation is examined numerically with the variations in the non-dimensional numbers. These results are shown with the help of graphs and briefly explained in the discussion. An analytical exploration is described for the unsteadiness parameter on the thin film. The larger values of the unsteadiness parameter increase the velocity profile. The nanofluid film velocity shows decline due the increasing values of the magnetic parameter. Moreover, a survey on the physical embedded parameters is given by graphs and discussed in detail.

Keywords: entropy generation; second-grade fluid; nanofluid; liquid films; thin film; time depending stretching surface; magnetic field; HAM

1. Introduction

In the last few years, thin film flow problems have received great attention. The history behind such a loyalty and importance is the use of thin film flow in various technological disciplines. Thin film flow problems cannot be categorized and classified in a simple way, because they are rooted in particular to broad areas, such as from the analysis of flow in human lungs to industrial problems involving lubricants. Examining thin film flow of liquids and its uses leads us to an important relationship between structural mechanics and fluid mechanics. The polymers and metal extraction, drawing of elastic sheet, exchanges, foodstuff striating, fluidization of the devices, and constant forming are some common uses and applications of liquid film flow. In view of these practical uses of liquid film flow, further advancement and development is observed to be necessary. For this purpose, a variety of attempts have been made with constructive geometries from time to time by many investigators. One such an important geometry is the expanding sheet, which has received great attention and become a problem of interest for the investigators [1,2].

In the beginning, thin liquid film flow was devoted to fluids with some viscosity. Classifications of these fluids based on viscosity have made the area saturated. With the passage of time, the domain was extended to non-Newtonian fluids. Non-Newtonian nano-liquids are studied and are discussed with variations in internal and external agents. The transfer of heat is investigated for non-Newtonian nanoliquid thin film flow by Sandeep et al. [3]. In stretching sheet problems, the geometry of the problem is important, due to its time dependency as well as the nature of the sheet. Wang [4] investigated the liquid thin film flow past a time-dependent expanding sheet. The same geometry with finite thin liquid is investigated by Usha et al. [5]. They analyzed the flow on an unsteady stretching sheet for finite thin liquids. Liu et al. [6] investigated the thin film flow for heat transfer enhancement through an expanding sheet. Aziz et al. [7] described the flow of thin fluid film with generation of heat over an expanding surface. Tawade et al. [8] examined thin film liquid flow for the transfer of heat in the presence of thermal radiations. They implemented the RK-Fehlberg and Newton-Raphson method to tackle the modeled equations. A briefer survey on heat transfer analysis on liquid film flow past an expanding sheet is presented by Andersson et al. [9]. The study of expanding sheet problem is not rare in the literature and a brief survey can be found on its applications and other technological advancements in [10–15]. Besides all these, a variety of fluids are investigated under the same geometry. Megahed [16] studied the impact of heat on thin Casson fluid past an unsteady expanding surface by assuming the slip velocity in the presence of viscous dissipation and heat flux. Shah et al. [17] described the flow of Casson nanofluid in rotating parallel plates in the presence of Hall effect. Jawad et al. [18] studied the MHD flow of the nanofluid thin film by considering the Joule heat loss and Navier's partial slip by considering Darcy-Forchheimer model. Interested readers are referred to [19–22] for more brief discussion on rotating systems. Some new modifications are made by Khan et al. [23] and Tahir et al. [24] for the thin film flow of nanofluids.

The proficiency in different applications of nanofluids are due to the enormous features (heat transfer enhancement, cooling etc.). From the practical application point of view, nanofluids are used in powered engines, pharmaceutical procedures, micro-electrons, and hybrid fuel cells. Presently, its major use is in the field of nanotechnologies. In industries, the use of electronic equipment and nanoboards are essential presently. These boards and electronic accessories become hot with the passage of time, due to which its efficiency is normally badly affected. To overcome this situation, nanofluids are used as a coolant to reduce heat [25]. A literature survey shows that air is used as a coolant in many processes. In the enhancement of the performance of microchips, projectors and LED nanotechnology coolants are used [26,27]. Non-Newtonian fluid flow is found in abundance in the literature and deeply depends on the mechanism in which it is used. One such a mechanism is the peristaltic mechanism, which plays a vital role in physiological and industrial processes. In this process, along the wall of the channel sinusoidal waves are propagated. The best examples of such waves in practice are dialysis, hose pumps, and the heating of lungs etc. Further investigation of this study leads researchers to examine MHD flows. MHD analysis of peristaltic flows plays a key

role in medicine and bio-engineering. The variations in viscosity for peristaltic flow are examined by Srivastava et al. [28]. The variation of viscosity with temperature is studied by Abbasi et al. [29] for nanofluid flow.

From earlier study, nanofluids have been found to retain dimensions smaller than 100 nm [7,8]. Nanofluids are known to be a mixture of nanoparticles and the general heat transfer fluids, for example oil, ethylene glycol, glycol, and water etc. Nanoparticles can be prepared in laboratories and in industries on a large scale. It can be obtained from metals such as Ag, Al, Au, Cu, and oxides of metals such as Fe_3O_4 , CuO, TiO_2 , Al_2O_3 , nitrides such as AlN, SiN, carbides (SiC) etc. The nanoparticles obtained from these materials are used in very small amounts for the improvement of heat transfer, due their high thermal conductivity. The enhancement of heat transfer due to thermal systems for augmentation are presently become widespread. Abolbashari et al. [30] described nanofluid flow using Buongiorno's model through a time-dependent stretching sheet. Hayat et al. [31] discussed the nanofluid flow in three dimensions by using the Maxwell model. Malik et al. [32] studied a mixed convective MHD nanofluid flow on a stretching surface by considering Eyring-Powell fluid. Nadeem et al. [33] discussed the Maxwell liquid film flow of nanoparticles past a perpendicular stretching surface. Raju et al. [34] examined the non-Newtonian nanofluid MHD flow through a cone with free heat convection and mass transfer. The heat transfer investigations of the nanofluid flow through plates are performed by Rokni et al. [35]. Numerical investigations of the non-Newtonian nanofluid flow on the stretching surface are presented by Nadeem et al. [36]. Shehzad et al. [37] examined the nanofluid MHD flow of Jeffrey fluid in the presence of convective-type boundary constraints. Sheikholeslami et al. [38,39] analyzed the heat effects on nanofluid flow by applying an external magnetic field. Mahmoodi et al. [40] studied the flow of nanofluid for cooling purposes and discussed the heat sink for the flow field. The impact of thermal radiations and Hall current is recently explored by Shah et al. [41,42] for rotating surfaces. A detailed study on rotating surfaces with stretching sheet performed by Shah et al. can be found in [43–49]. CuO containing nanofluid thin film flow inside a semi-annulus region is examined by Sheikholeslami and Bhatti [50] numerically with constant magnetic field. They analyzed the heat transfer enhancement and found some good results. Tube-in-tube analysis of heat exchanger for γ -ALOOH nanofluid is performed by Monfared et al. [51]. They found both upper and lower boundaries of irreversibility for platelet and spherical shape geometries. A brief and detailed survey on nanofluids of Sheikholeslami with modern applications of dissimilar phenomena with a variety of approaches can be found in [52,53]. Besides the theoretical study, literature is rich with experimental results on nanofluid flow and its use in the heat transfer analysis. A combined effect of the silver and carbon nanotubes by taking water as the base fluid is performed by Munkhbayar [54]. In this study, he used 3% of the nanoparticles by volume as compared with base fluids. The use of these combined nanoparticles enhances the heat transfer up to 14.5% at a very low temperature. The increase in concentration and heat transfer for a hybrid of the copper oxide and titanium nanoparticles is achieved by taking water and ethylene glycol mixture as the base fluid studied by Hemmat et al. [55]. They performed this experiment in a laboratory from (30–60)°C. At the upper bound of the temperature range they found a 41.5% increase in the thermal conductivity. Hybrid base fluid (water-ethylene) and hybrid nanofluids (titanium-MWCNT's) investigation was carried out by Akhgar et al. [56] for the stability of base fluid and enhancement of thermal conductivity. They observed a 38.7% increase in the thermal conductivity of the nanofluids as compared with the base fluid. Similar experimental results for the enhancement of the thermal conductivity of nanofluids can be found in [57,58].

The free existence of non-Newtonian fluids and its use attracted researchers to construct models and further developments due to its application in industry. Most of the organic compounds came under the umbrella of the non-Newtonian fluids. Food products, molten plastic, wall paints, lubricant oils, drilling mud, and molten plastic are some of the widely used examples non-Newtonian fluids. Surveys suggest that to classify the non-Newtonian fluids in terms of behavior, many models have been introduced and developed. Some of them, Williamson fluid, Walter's-B fluid, Casson fluid,

Carreau fluid, etc., are very common in use. Carreau fluid model is also known as the Newtonian generalized model [59]. The significance of the Carreau fluid model in the field of melts, water-based polymers, and suspensions attracted investigators. Considering the effectiveness of this model, many researchers investigated the nature of Carreau fluid by using different geometries. Some surveys related to this model are presented here. Kefayati et al. [60] performed a survey on the thermosolutal forced convective flow over two circular cylinders with magnetic effects by taking the Carreau fluid model. They also analyzed the entropy generation in their study. Olajuwon [61] studied the Carreau liquid flow over a perpendicular permeable surface with magnetic effect. Hayat et al. [62] investigated this model for a free convection flow over a non-stationary surface. The study of nanofluids is not just linked to the fluids model used, but purely depends on the nature of the nanomaterial used. The shape of the nanomaterial used is more important in the study of heat transfer processes. To enhance the heat transfer, and to improve thermal and hydraulic properties, the shape of the nanoparticles used is also important. Alsarraf et al. [63] implemented a two-phase mixture model to investigate the double-pipe flow of boehmite alumina nanofluid. They presented the results in the form of percentages for both spherical and platelet-shaped nanoparticles under high Reynolds numbers. Similarly, an experimental study is presented by Azari et al. [64] for alumina nanofluid flow. They successfully analyzed the two-phased model theoretical results with practically obtained information.

Due to its complicated nature, non-Newtonian fluids have been studied by many researchers, just for the purpose of explicitly or implicitly explaining the strain rate. An important type of non-Newtonian fluids is Sisko fluid, which has great significance in engineering as well as in technology. Stretching surface analysis was made by Munir et al. [65] by using Sisko fluid bidirectional flow. Sisko model is used by Olanrewaju et al. [66], for the unsteady non-convective fluid flow over a flat surface by taking into account heat transfer. Khan et al. [67] studied the effect of heat energy transfer in an annular pipe of the Sisko fluid steady state flow. Khan et al. [68] described the Sisko fluid boundary-layer flow over a stretching surface. Similar investigation on the stretching surface for the laminar flow by using Sisko fluid model is carried out by Patel et al. [69]. Darji et al. [70] examined the natural convective time-independent Sisko fluid flow of boundary-layer type. Analytical solutions of the Sisko fluid thin film flow for the drainage down a vertical belt is presented by Siddiqui et al. [71]. The MHD Sisko fluid numerical study for an annular region flow is carried out by Khan et al. [72]. Sar et al. [73] studied both the Lie group and Sisko fluid boundary-layer equations. Haneef et al. [74] investigated the Maxwell nanofluid flow for magnetic and electric effects on a stretching plate. Moallemi et al. [75] studied the flow of Sisko fluid in the pipe and discussed the exact solution. Dawar et al. [76] investigated the CNT Casson fluid flow with MHD in a rotating channel for heat transfer analysis. Shah et al. [77] implemented Cattaneo-Christov model for the heat transfer analysis of MHD micropolar Casson fluid over a stretching sheet. Khan et al. [78] investigated the Eyring-Powell nanoliquid film slip flow by considering nanoparticles of graphene. Recently, Khan and Pop [79] investigated the thermophoresis effect and Brownian motion of a boundary-layer nanofluid flow past a stretching sheet. For the enhancement of heat transfer, researchers started to use impurities. Osiac [80] discussed the electrical and structural properties of nitrogen. Radwan et al. [81] performed the synthesis classification and applications of polystyrene. Coating applications of thin film flow and flexible coating with conductive fillers and applications of thermoelectric materials are discussed [82–85].

The best possible design conduction in the energy system is always the aim of investigators. For this purpose, the role of entropy cannot be ignored in modeling, and other optimization applications of the energy systems. The roots of entropy are connected to the second law of thermodynamics and its irreversible aspects are laid down by Kelvin and Clausius. The theoretical background of entropy was developed very rapidly and has been extended to the new generation. However, in the heat transfer process/thermal radiations, entropy generation cannot be treated by conventional thermodynamic approaches. That is why researchers are compelled to take an interest in the second law of thermodynamics and to investigate its engineering applications. When there is a heat transfer in the system, there must be the generation of entropy. The generation of entropy is

mainly concerned with the irreversibility of thermodynamics. Entropy can be generated from different sources, such as viscous dissipation, mass diffusion, and finite temperature gradients in the transfer of heat. The generation of entropy in thermal engineering has been investigated by Bejan [86,87] from some new aspects. The work already available in the system vanishes due to the generation of entropy. From an engineering point of view, it makes sense to understand the irreversibility and mechanism of the entropy generation in the transfer of heat and other problems in the fluid flow.

The generation of entropy in thermal systems has been discussed by many investigators. Weigand and Birkefeld [88] investigated the laminar flow past a flat plate with entropy generation. Makinde [89] investigated the second law for the hydro-magnetic flow of the boundary layer on a stretching surface along with the heat transfer analysis by using variable viscosity. Makinde reported that with the increasing values of Prandtl number and radiation parameter the entropy generation decreases. Hayat et al. [90] presented Darcy-Forchheimer CNT-based nanomaterial convective flow with heat flux for entropy generation. They analyzed both SWCNTs and MWCNTs for heat transfer enhancement and entropy generation. In another investigation of gravity-driven thin film flow in the direction of the heated inclined plate, Makinde [91] reported that at the liquid-surface, the irreversibility of heat transfer is dominant, while an opposite result is observed at the surface of the plate. A small amount of work is done on the heat transfer analysis, considering the second law of thermodynamics in nanofluids. This is because of the rareness of the nanofluids. Recently, Esmailpour and Abdollahzadeh [92] investigated the enhancement of heat for nanofluid free convection flow inside an enclosure with the entropy generation. Dawar et al. [93] presented a semi-analytic solution to the CNT nanofluid flow inside rotating plates. In this investigation, the effect of magnetic field and entropy generation is deliberated numerically. A further brief survey on entropy generation by investigating different models and geometries can be found in [94,95]. Surveys suggest that the stretching sheet problem has been studied by different researchers for different fluids. Entropy generation of viscoelastic fluid for the second-grade fluid is rare and will be discussed in this article for the first time. In science and engineering majority of the mathematical models are very complicated, and it is also impossible to solve these types of problems for exact solution. For this purpose, researchers are widely using numerical and semi-analytic methods for the approximate solution. Numerical techniques are sometimes difficult to perform in an efficient way for some problems. This happens due the high non-linearity of the problem. To overcome this situation, Liao [96,97] investigated the solution of these types of problems by implementing a new technique. The method is termed the Homotopy Analysis Method (HAM), due to the use of homotopy, a topological property. He further discussed the convergence of the new implemented method. A solution is a function of single variable in the form of a series.

The foremost aim of discussing this work is to investigate the flow of second-grade thin film flow in the presence heat transfer and magnetic effect with the generation of entropy in a vertical stretching sheet. To the best of our knowledge, we cannot find new work on nanofluid thin film flow on vertical stretching sheet by considering viscoelastic fluid of second grade. Equations for the generation of entropy and the boundary-layer heat transfer over a vertical stretching sheet are constituted for two-dimensional nanofluid thin film flow with uniform magnetic field (MHD). These equations are the leading-order mathematical equations constituted from the geometry, keeping in view the assumptions in flow field. Different physical aspects such as thermophoresis, concentration gradients, and Brownian motion of the flow are assumed in the nanofluid model. The modeled leading-order system in the form of PDEs (partial differential equations) are further transformed into a system of ODEs (ordinary differential equations), with the help of similarity variables. Similarity variables have the property of non-dimensionalization and transforming the system of PDEs to a single independent variable system also known as ODEs. The reduced system of differential equations is tackled by an analytic approach (HAM). HAM is implemented with initial guesswork, as required for the implementation of the technique, due to its fast convergence. The convergence of the implemented technique is discussed numerically and with graphs. The state variables are plotted under the variation of different physical parameters and discussed in detail. Physical quantities such as Sherwood number, Nusselt number,

and skin friction are presented numerically for its significance in the boundary-layer flow. The impact of Brinkman number and Bejan number is discussed by graphs for entropy function. The effect of Reynolds number, Prandtl number, and magnetic parameter is also influential on entropy function, Bejan number, and Brinkman number by graphs.

2. Problem Formulation

Assume an unsteady nanoliquid thin film flow of the second-grade fluid past a stretching sheet. Furthermore, the fluid is assumed to be electrically conducting and the magnetic field effect is also considered inside the flow field. The moving sheet starts its motion from a fixed slit. The arrangement of the geometry is made in the Cartesian system of coordinates in such a way that the plate length is equal to ox , and oy is flat to the surface. The stretching effects are applied in such a manner to the surface of the flow that the two forces are in opposite direction with an equal magnitude along the x -axis, and keeps the center motionless. The stretching sheet and x -axis are taken in such a manner that it is adjacent to each other, and the stress velocity of the sheet is given by [17]:

$$U_w(x, t) = \gamma x(1 - \zeta t)^{-1}, \quad (1)$$

where ζ and γ represents any fix numbers, which are vertical to x -axis. The wall temperature and capacity of the nanoparticles are given by [17,19]:

$$T_w(x, t) = T_r \left(\frac{\gamma x^2}{2\nu_f} \right) (1 - \zeta t)^{-1.5} + T_0 \quad (2)$$

$$C_w(x, t) = C_r \left(\frac{\gamma x^2}{2\nu_f} \right) (1 - \zeta t)^{-1.5} + C_0 \quad (3)$$

where ν_f denotes the fluid kinematic viscosity, T_0 and C_0 denotes the temperature of the slit and volume friction of the nanoparticles, while T_r and C_r represents the reference temperature and reference volume of the nanoparticles, respectively.

The applied magnetic field has the relationship of the form [17]:

$$B(t) = B_0(1 - \zeta t)^{-\frac{1}{2}}, \quad (4)$$

here B_0 is the magnetic field strength.

The mathematical model that illustrates the second-grade fluid is given in the form [23]:

$$\vec{T} = -p\vec{I} + \vec{S}. \quad (5)$$

The basic equations of the second-grade fluid can be obtained by using $\beta_1 = \beta_2 = \beta_3 = 0$ in the third-grade fluid model *i.e.*

$$\vec{S} = \tau = \mu \vec{A}_{(1)} + \alpha_{(2)} \vec{A}_{(2)} + \alpha_{(2)} \vec{A}_{(2)}^2. \quad (6)$$

Here $p\vec{I}$ is an isotropic stress, \vec{S} is an extra tensor of stress, μ is the coefficient of viscosity, $\alpha_{(1)}$ and $\alpha_{(2)}$ represent the thermal stress moduli, $\vec{A}_{(1)}$ and $\vec{A}_{(2)}$ are the stresses of Rivlin Ericksen tensors and have the mathematical structures $\vec{A}_{(1)} = \nabla \vec{V} + (\nabla \vec{V})^T$ and $\vec{A}_{(2)} = \frac{D}{Dt}(\vec{A}_{(1)}) + \vec{A}_{(1)} \nabla \vec{V} + (\nabla \vec{V})^T \vec{A}_{(1)}$

2.1. Continuity Equation:

The equation of continuity under the assumed assumption (in-compressible fluid) for the modeled geometry takes the vectorial form [74]:

$$\nabla \cdot \vec{V}. \quad (7)$$

For two-dimensional nanofluids, Equation (7) takes the form:

$$\frac{\partial u}{\partial x} + \frac{\partial v}{\partial y} = 0 \quad (8)$$

2.2. Momentum Equation

The momentum equations for the modeled geometry and flow assumptions, are given by [74]:

$$\rho \frac{D}{Dt}(\vec{V}) = \nabla \cdot \vec{T} + \vec{J} \times \vec{B} + \vec{g}. \quad (9)$$

Here ρ denotes the fluid density, \vec{V} velocity, which can be expressed in components form as: $\vec{V} = (u, v, 0)$, \vec{T} Cauchy tensor of stress and \vec{g} force acts from a distance respectively. $\vec{J} \times \vec{B}$ represents the famous Lorentz force, in which \vec{J} is the current density, B is the magnetic field with a magnetic field strength B_0 . Furthermore, \vec{J} can be expressed as: $\vec{J} = \sigma(\vec{E} + \vec{V} \times \vec{B})$, also known as Ohm's law, in which σ and \vec{E} describe the electrical conductivity and electric field respectively, and assume that $\vec{E} = 0$. $\frac{D}{Dt}$ represents the substantial derivative. Using all the above assumptions in Equation (9), we get

$$\frac{\partial u}{\partial t} + u \frac{\partial u}{\partial x} + v \frac{\partial v}{\partial y} - \nu \frac{\partial^2 u}{\partial y^2} = \frac{\alpha_1}{\rho} \left(\frac{\partial}{\partial y} \left(u \frac{\partial^2 u}{\partial y^2} \right) - \frac{\partial u}{\partial y} \frac{\partial^2 u}{\partial x \partial y} + \nu \frac{\partial^2 u}{\partial y^2} \right) - \sigma B_0^2 u + g_r \beta_T (T - T_\infty) + g_c \beta_T (C - C_\infty), \quad (10)$$

where B_0 and α_1 describe the strength the magnetic field and thermal conductivity of the fluid, respectively, β_T is the thermal expansion coefficient, C_∞ and T_∞ denotes the concentration and temperature at a distance from the surface, and g is the gravitational acceleration.

2.3. Equation of Thermal Energy

Thermal energy equation for the unsteady flow field is presented in the form [74]:

$$\frac{\partial T}{\partial t} + \vec{V} \cdot \nabla T = \nabla \cdot \left[\frac{K(T)}{(\rho c_p)_f} \nabla T \right] + \tau \left[D_B \nabla C \cdot \nabla T + \left(\frac{D_T}{T_0} \nabla T \cdot \nabla T \right) \right], \quad (11)$$

where T represents the temperature, $\tau = \frac{\rho_p}{\rho_f}$ illustrates the ratio of the base liquid to thermal capacities of nanoparticles, the heat capacitance of the liquid is represented by c_p , D_B represents the constant of Brownian diffusion, while D_T demonstrates the constant of thermophoretic diffusion, T_0 denotes the liquid temperature, which is detached from the sheet.

After implementing the assumptions (two-dimensional, unsteady, viscous, in-compressible, electrically conducting, etc.), Equation (11) is reduced to:

$$\frac{\partial T}{\partial t} + u \frac{\partial T}{\partial x} + v \frac{\partial T}{\partial y} = \frac{1}{\rho c_p} \frac{\partial}{\partial y} \left[\frac{\partial u}{\partial y} \right] + \tau \left[D_B \left(\frac{\partial C}{\partial y} \frac{\partial T}{\partial y} \right) + \frac{D_T}{T_\infty} \left(\frac{\partial T}{\partial y} \right)^2 \right]. \quad (12)$$

2.4. Equation of Mass Transfer

The nanofluid concentration can be mathematically described as [14]:

$$\frac{\partial C}{\partial t} + \vec{V} \cdot \nabla C = D_B \nabla^2 C + \frac{D_T}{T_0} \nabla^2 T. \quad (13)$$

After applying the assumptions, Equation (13) takes the form:

$$\frac{\partial C}{\partial t} + u \frac{\partial C}{\partial x} + v \frac{\partial C}{\partial y} = D_B \frac{\partial^2 C}{\partial y^2} + \frac{D_T}{T_\infty} \left(\frac{\partial^2 T}{\partial y^2} \right). \quad (14)$$

The pertinent restrictions can be written as:

$$u = U_w, \quad v = 0, \quad T = T_w, \quad C = C_w \quad \text{at} \quad y = 0, \quad (15)$$

$$\frac{\partial u}{\partial x} = \frac{\partial T}{\partial x} = \frac{\partial C}{\partial x} = 0, \quad v = \frac{dh(t)}{dt}, \quad C > 0, \quad \text{at} \quad y = h. \quad (16)$$

Introducing the following transformations [14]:

$$\begin{aligned} \psi &= x \sqrt{\frac{v\gamma}{1-\zeta t}} f(\eta), \quad u = \frac{\partial \psi}{\partial y} = \gamma x \frac{f'(\eta)}{1-\zeta t}, \quad v = \frac{\partial \psi}{\partial x} = -\sqrt{\frac{\gamma v}{(1-\zeta t)}} f(\eta), \\ \eta &= \sqrt{\frac{\gamma}{v(1-\zeta t)}} y, \quad h(t) = \left[\frac{v}{\gamma(1-\zeta t)^{-1}} \right]^{\frac{1}{2}}, \quad \theta(\eta) = \frac{T - T_0}{T_w - T_0}, \quad \phi(\eta) = \frac{C - C_0}{C_w - C_0}. \end{aligned} \quad (17)$$

Here the stream function is represented by ψ , the thickness of the fluid film is denoted by $h(t)$, and the kinematic viscosity is represented by $\nu = \frac{\mu}{\rho}$. The dimensionless film thickness is defined as:

$$\beta = \sqrt{\frac{\zeta}{v(1-\zeta t)}} h(t) \quad (18)$$

In other words, Equation (18) becomes:

$$\frac{dh}{dt} = -\frac{\zeta \beta}{2} \sqrt{\frac{v}{\zeta(1-\zeta t)}}. \quad (19)$$

With the help of the newly introduced variables, Equations (10)–(14) are reduced to the following equations, while the continuity equation is satisfied identically.

$$f''' + \gamma_1 (f''' f' - (f'')^2 - f f^{iv}) + f f'' - (f')^2 - St (f' + \frac{\eta}{2} f'') - Gr\theta + Gm\phi + Mf' = 0, \quad (20)$$

$$(1 + Rd)\theta'' + f\theta' - 2f'\theta - \frac{St}{2}(3\theta + \eta\theta') + Nt(\theta')^2 + Nb\theta'\phi' = 0, \quad (21)$$

$$\phi'' + Sc [f\phi' - 2f'\phi - \frac{St}{2}(3\phi + \eta\phi')] + \frac{Nt}{Nb}\theta'' = 0. \quad (22)$$

The boundary conditions of the problem are:

$$f(0) = 0, \quad f'(0) = 1, \quad \theta(0) = 1, \quad \phi(0) = 1, \quad f(\beta) = \frac{S\beta}{2}, \quad f''(\beta) = 0, \quad \theta'(\beta) = 0, \quad \phi'(\beta) = 0. \quad (23)$$

After generalization, the physical parameters are defined as: $St = \frac{\gamma}{\epsilon}$ is the measure of the time-dependent non-dimensional parameter, $\gamma_1 = \frac{\alpha_1 \beta^2}{\rho \delta^2}$ is the second-grade fluid stretching parameter, $M = \frac{\sigma_f B_0^2}{b \rho_f}$ represents the magnetic parameter, $\lambda = m(T - T_0)$ denotes the variable viscosity, $Pr = \frac{\rho v c_p}{k}$ represents the Prandtl number, $Nt = \frac{\tau D_w (T_w - T_\infty)}{v T_\infty}$ demonstrates thermophoresis parameter, $Nb = \frac{\tau D_B (C_w - C_\infty)}{v}$ represents the limitations of Brownian motion, $Gm = \frac{g \beta L^3 (C_w - C_\infty)}{v}$ is the mixing parameter, $Gr = \frac{g \beta L^3 (T_w - T_\infty)}{v}$ denotes the Grashof number, $Rd = \frac{16 \sigma T_\infty^3}{3 k k^*}$ is the radiation parameter, and $Sc = \frac{v}{D_B}$ represents Schmidt number.

3. Parameters of Interest

3.1. Skin Friction

The coefficient of skin friction can be defined in the closed form as:

$$C_f = \frac{(\vec{S}_{xy})_{y=0}}{\frac{\rho U_w^2}{2}}, \quad (24)$$

where

$$\vec{S}_{xy} = \left[\mu \frac{\partial u}{\partial y} + \rho a_1 \left(2 \frac{\partial u}{\partial x} \frac{\partial u}{\partial y} + \frac{\partial^2 u}{\partial x \partial y} \right) \right] \quad (25)$$

A dimensionless description of C_f is demonstrated as:

$$C_f = (Re_e)^{-\frac{1}{2}} (f''(0) + 3\gamma_1 f''(0) f'(0)), \quad (26)$$

where Re_e denotes the local Reynolds number, and has the mathematical description given as: $Re_e = \frac{U_w x}{\nu}$.

3.2. Nusselt Number

Nusselt number has the closed mathematical form given by $Nu = \frac{h Q_w}{k(T_0 - T_h)}$, where $Q_w = -\hat{k} \left(\frac{\partial T}{\partial y} \right)_y = 0$, and is known as the flux of heat. A dimensionless description of Nu is demonstrated as:

$$Nu = -\Theta(0) \quad (27)$$

3.3. Sherwood Number

Sherwood number can be demonstrated in mathematical form as: $Sh = \frac{h J_w}{D_B(C_0 - C_h)}$, where $J_w = -D_B \left(\frac{\partial C}{\partial y} \right)_{y=0}$ is the flux of mass. The non-dimensional descriptions of Sh is demonstrated as:

$$Sh = -\Phi(0) \quad (28)$$

4. Entropy Analysis and Its Mathematical Description

Entropy generation of volumetric type of viscous fluids is demonstrated as [87,88]:

$$S''' = \frac{K(T)}{T_0^2} \left[\left(\frac{\partial T}{\partial y} \right)^2 + \frac{16\sigma T_\infty^3}{3k} \left(\frac{\partial T}{\partial y} \right)^2 \right] + \frac{\mu(T)}{T_0} \left(\frac{\partial u}{\partial y} \right)^2 + \frac{Rd}{C_0} \left(\frac{\partial C}{\partial y} \right)^2 + \frac{Rd}{T_0} \left(\frac{\partial T}{\partial y} \frac{\partial C}{\partial y} + \frac{\partial C}{\partial x} \frac{\partial T}{\partial x} \right) + \frac{\sigma B_0^2 u^2}{T_0} \quad (29)$$

Equation (29) illustrates that the entropy generation has two main features, i.e., the irreversibility of the transmission of heat, and the fluid friction irreversibility. Magnetic and porosity effects are illustrated in the last two terms. The aspects of entropy generation are illustrated by mathematical description, given by

$$S_0''' = \frac{K_0(\Delta T)^2}{L^2 T_0^2}, \quad (30)$$

while $N_G = \frac{S'''}{S_0'''}$, demonstrates the ratio of the actual entropy generation to the generation rate of characteristic entropy. This number N_G for a non-dimensional system takes the form:

$$N_G = Re(1 + \epsilon\theta + Rd)(\theta')^2 + \frac{Re Br}{\Omega(1 + \Lambda)} (f'')^2 + \frac{Re Br}{\Omega} M(f')^2 + Re\lambda \left(\frac{\chi}{\Omega} \right)^2 (\phi')^2 + Re\lambda \left(\frac{\chi}{\Omega} \right) \theta' \phi', \quad (31)$$

where Br is used for the Brinkman number, λ represents the diffusion quantity, M demonstrates the parameter of the magnetic field, Ω and χ denotes the dimensionless temperature and concentration change, respectively.

The illustrated mathematical description of each parameter is given as:

$$Re = \frac{bL^2}{\nu}, \Omega = \frac{\Delta T}{T_0}, \chi = \frac{\Delta C}{C_0}, \lambda = \frac{RdC_0}{k}. \quad (32)$$

The source of the generation of the entropy is an important class for engineers, the Bejan number is responsible for such an important measurement, which is defined as:

$$Be = \frac{\frac{K(T)}{T_0^2} \left[\left(\frac{\partial T}{\partial y} \right)^2 + \frac{16\sigma T_\infty^3}{3k} \left(\frac{\partial T}{\partial y} \right)^2 \right]}{\frac{\mu(T)}{T} \left(\frac{\partial u}{\partial y} \right)^2 + \frac{\sigma B_0^2 u^2}{T}} \quad (33)$$

The alternative representation of the Bejan number Be , after using the similarity transformations, is:

$$Be = \frac{(1 + \epsilon\theta + Rd)(\theta')^2}{\frac{Br}{\Omega(1+\Lambda)}(f'')^2 + \frac{Br}{\Omega}M(f')^2} \quad (34)$$

5. Solution by HAM

Numerical methods applied presently uses the concept of linearization and discretization to tackle the nonlinear systems. HAM is the method used for the same purpose, analytically, as the numerical techniques. Its derivation is totally dependent on the topological concept known as homotopy. Liao [97,98] was the first to use this concept successfully. For this purpose, Liao used the idea of homotopy by considering two continuous functions Ψ_1 and Ψ_2 defined on the topological spaces \bar{X} and \bar{Y} . The homotopic idea explained in topological spaces is implemented over a closed unit interval by:

$$\Psi : \bar{X} \times [0, 1] \rightarrow \bar{Y}$$

where the relation holds for all $\bar{x} \in \bar{X}$, together with $\Psi[\bar{x}, 0] = \zeta_1(\bar{x})$ and $\Psi[\bar{x}, 1] = \zeta_2(\bar{x})$. The mapping defined by Ψ is known as a homotopic function in the literature. Equations (20)–(23) have been tackled by HAM. Solutions are restricted by a new parameter, \hbar , which modifies and links the solutions in an appropriate manner.

We guess

$$f_0(\eta) = \frac{1}{4\beta^2}(4\beta^2\eta + 3\beta(S-2)\eta^2 + (2-S)\eta^3), \quad \theta_0(\eta) = 1, \quad \phi_0(\eta) = 1. \quad (35)$$

The linear operators represented by $L_{\tilde{f}}$, $L_{\tilde{\theta}}$ and $L_{\tilde{\phi}}$ are defined as:

$$L_{\tilde{f}}(\tilde{f}) = \tilde{f}''', \quad L_{\tilde{\theta}}(\tilde{\theta}) = \tilde{\theta}'', \quad \text{and} \quad L_{\tilde{\phi}}(\tilde{\phi}) = \tilde{\phi}'', \quad (36)$$

with the following properties

$$L_{\tilde{f}}(a_1 + a_2\eta + a_3\eta^2) = 0, \quad L_{\tilde{\theta}}(a_4 + a_5\eta) = 0, \quad \text{and} \quad L_{\tilde{\phi}}(a_6 + a_7\eta) = 0. \quad (37)$$

6. HAM Solution Convergence

The goal of the HAM solution (series solution) is its convergence, which is always linked to some constraints. The subordinate restrictions $\hbar_{\tilde{f}}$, $\hbar_{\tilde{\theta}}$, and $\hbar_{\tilde{\phi}}$ are implemented in the HAM procedure. The embedding parameters choice guarantee the solution convergence [99]. In our case, the proposed method shows the performance in the form of results, which are valid and efficient. The probability

sectors of \hbar are constructed \hbar -curves of $\tilde{f}''(0)$, $\tilde{\theta}'(0)$ and $\tilde{\phi}'(0)$ for the HAM solution (approximated) of order 25. The effective domains of \hbar are $-1.5 < \hbar_{\tilde{f}} < 0.0$, $-1.5 < \hbar_{\tilde{\theta}} < 0.0$ and $-2.5 < \hbar_{\tilde{\phi}} < 0.0$. Figure 1 illustrates the HAM technique convergence of \hbar -curves for the state variables (velocity, temperature, and concentration). The numerical values of HAM solution convergence with the variations of different parameters are presented in Tables 1 and 2. The table illustrates that HAM is a rapidly convergent method.

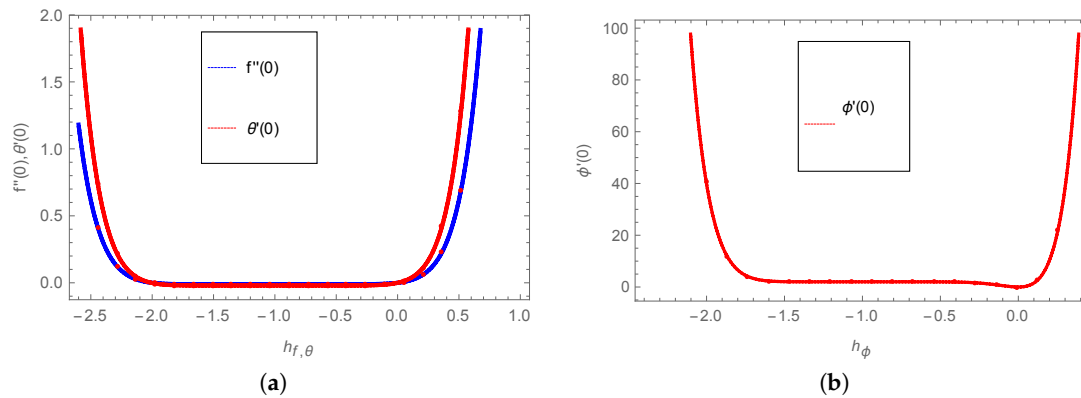


Figure 1. (a,b) \hbar -curve representation of $f(\eta)$, $\theta(\eta)$ and $\phi(\eta)$.

Table 1. 25th-order approximation table for HAM convergence, when $\gamma_1 = Sc = 0.5$, $Nt = Gr = \beta = St = 0.1$, $h = -0.5$, $Pr = Nb = Gm = 0.1$.

Approximation Order	$f''(0)$	$\Theta'(0)$	$\phi'(0)$
1	-0.0600000	-1.107500	0.0537500
3	-0.104656	-0.106980	0.0856833
5	-0.115692	-0.106849	0.0935671
7	-0.118420	-0.106817	0.0955156
9	-0.119090	-0.106809	0.0095997
11	-0.119261	-0.106807	0.0961163
13	-0.119303	-0.106807	0.0961457
15	-0.119313	-0.106806	0.0961530
17	-0.119315	-0.106806	0.0961548
19	-0.119316	-0.106806	0.0961552
23	-0.119316	-0.106806	0.0961554
25	-0.119316	-0.106806	0.0961554

7. Results and Discussion

The objective of our investigation focuses on the interpretation of the thin film flow of nanoliquid flow parameters. Figures 2–23 reveal the comprehension of the parameters involved in our model equations.

7.1. Velocity Profile

The liquid film thickness β along the direction of the fluid flow is illustrated in Figure 2. The flow velocity curve declines with the larger numbers of the film thickness β , because the dimensionless thin film thickness is directly related to the fluid thickness $h(t)$ and is the function of viscosity. As a result, an increase in β further increases the viscosity of the film, which further causes in the decline of the velocity curve. This happens due to the indirect relationship between β and the flow velocity profile, i.e., the increasing values of β decrease the viscosity of the fluid, which as a result decreases the velocity profile.

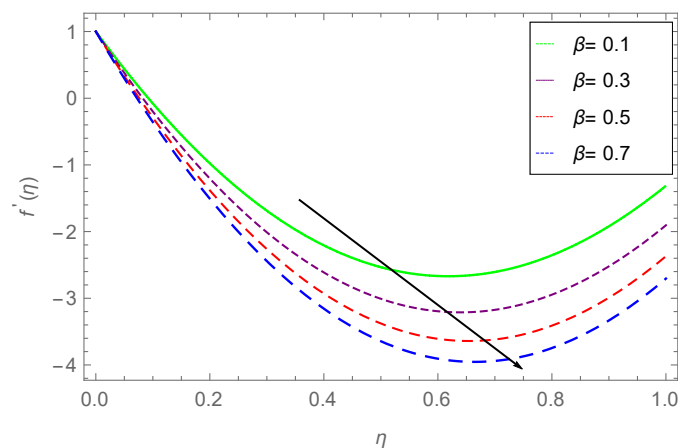


Figure 2. Impact of β on $f'(\eta)$, when $\gamma_1 = 0.2$, $St = 0.6$, $Gm = 0.8$, $Gr = 0.7$, $M = 0.8$.

Figure 3 reflects the impact of the unsteadiness parameter over the profile of the velocity for dissimilar values of the embedded parameters. A direct variation can be observed in the profile of the velocity with the variations in the unsteadiness parameter St in the figure as demonstrated. These variations are due to the effect of the stretching parameter. The unsteadiness parameter is a function of the liquid film thickness, which further varies directly with the stretching parameter and as a result increases the velocity profile. An increase in St rises the motion of the fluid. Investigation demonstrates that the solution exists for $St \in [0, 2]$ and strongly depends on the parameter St .

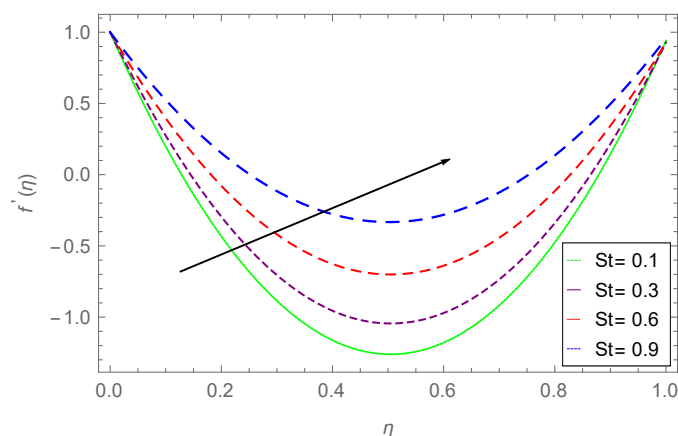


Figure 3. Impact of St on $f'(\eta)$, when $\gamma_1 = 0.2$, $\beta = 0.9$, $Gm = 0.8$, $Gr = 0.7$, $M = 0.7$.

Figure 4 illustrates the mixed convective effect on the flow. In Figure 4 Gm shows the characteristic of buoyancy forces, which play a favorable behavior for the state variable velocity. The mixing parameter is mainly affected by the length, concentration difference, and the kinematic viscosity of the nanofluid. There is an inverse relation between the velocity and the viscosity of the nanofluid. Therefore, when the mixing parameter increases, the liquid film concentration increases directly, and the viscosity decreases, which further causes increase of the profile of the velocity. The velocity profile shows a direct relation to Gm .

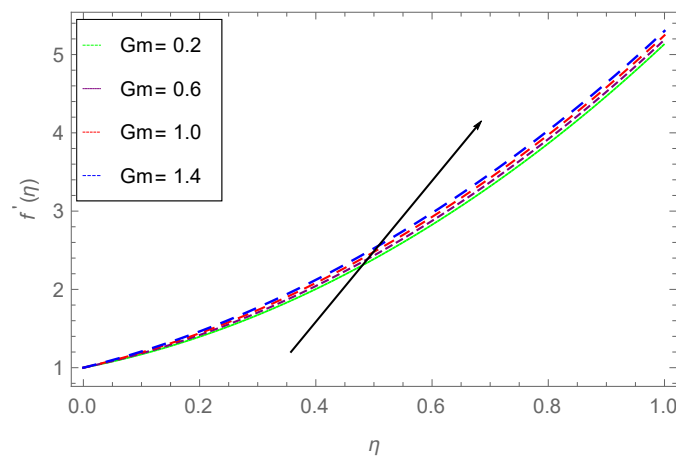


Figure 4. Impact of Gm on $f'(\eta)$, when $\gamma_1 = 0.2$, $\beta = 0.9$, $St = 0.3$, $Gr = 0.7$, $M = 0.9$.

Figure 5 reveals the effect of the order two-fluid velocity distribution parameter γ_1 . Physically, this parameter is inversely related to the density, keeping the thickness parameter constant. Therefore, an increase in the values of the parameter γ_1 , would decrease the density of the fluid, which further causes in the increase of the velocity profile. In other words, it would make the fluid less dense and as a result the fluid velocity jumps up. Thus, the larger the values of non-Newtonian parameter, the greater the motion of thin film.

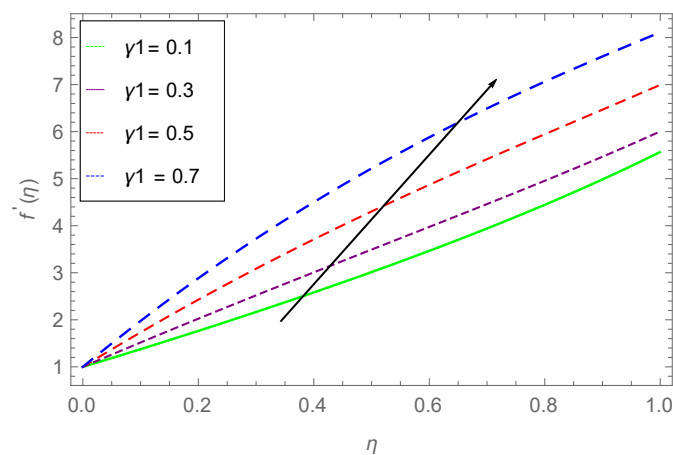


Figure 5. Impact of γ_1 on $f'(\eta)$, when $Gm = 0.8$, $\beta = 0.9$, $St = 0.3$, $Gr = 0.7$, $M = 0.7$.

Figure 6 illustrates the relation between Grashof parameter Gr and the profile of the velocity. Here Gr shows the characteristics of buoyancy forces, which offers a favorable behavior for the velocity profile. Physically, Grashof number Gr is the ratio of the buoyancy force to the viscous force. Increasing values of the buoyancy forces cause the decrease of the viscous forces, which as a result producing faster motion. In summary, the increasing values of Gr causes a rapid increase in the velocity profile.

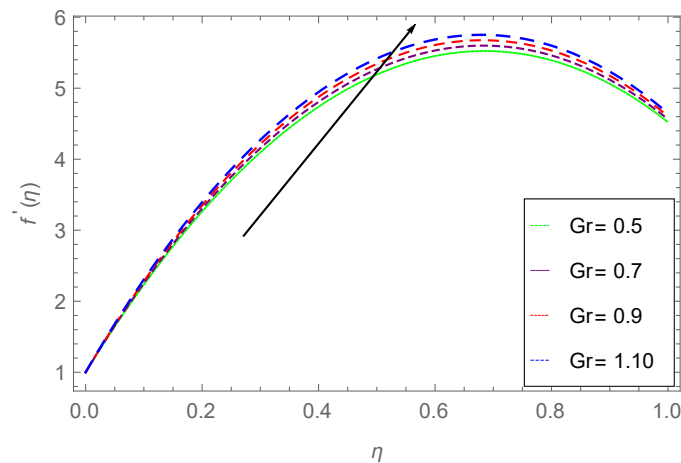


Figure 6. Impact of Gr on $f'(\eta)$, for $\gamma_1 = 0.4$, $\beta = 0.6$, $St = 0.5$, $Gm = 0.8$, $M = 0.7$.

Figure 7 illustrates the variation of the magnetic parameter M over the velocity profile. Since the magnetic parameter is applied horizontally to the surface on which the nanofluid flows, so an increase in the magnetic parameter would increase the strength of the magnetic field that create bending on the surface of the plate. This bending causes the decline of the velocity profile, but does nothing to the magnitude. In short, with the increasing values of the magnetic parameter M , a decrease is observed in the velocity profile.

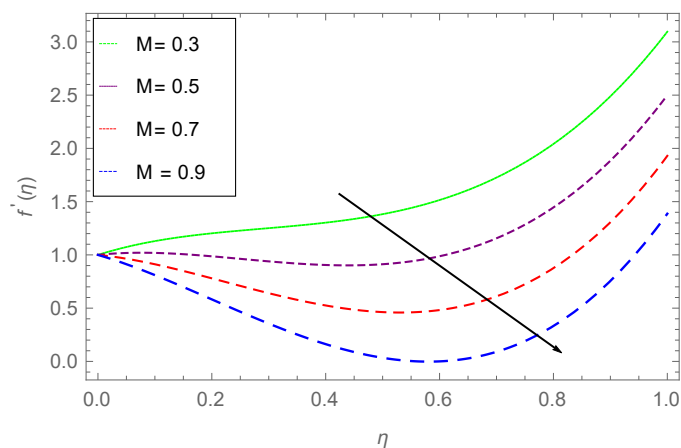


Figure 7. Impact of M on $f'(\eta)$, for $\gamma_1 = 0.2$, $\beta = 0.6$, $St = 0.6$, $Gr = 0.5$, $Gm = 0.8$.

7.2. Temperature Profile

The effect of thermal radiations Rd on $\theta(\eta)$ is discussed in Figure 8. The figure reveals an inverse relationship between the thermal radiation parameter Rd and the temperature profile. For higher values of Rd a rapid decrease can be observed in the profile of the temperature and vice versa.

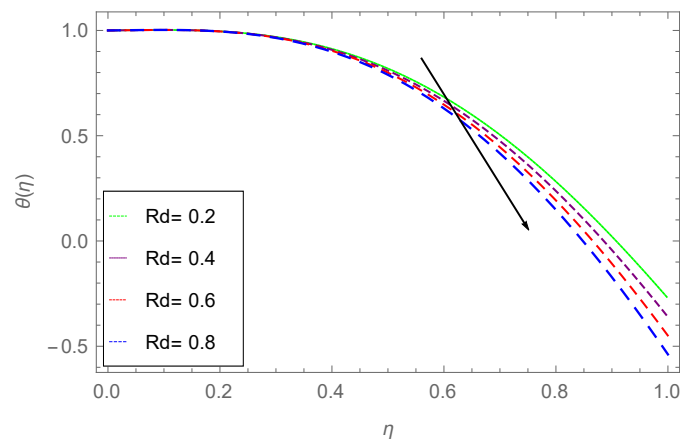


Figure 8. Impact of Rd on $\theta(\eta)$, for $\beta = 0.1$, $St = 0.1$, $Nt = 0.6$, $Nb = 0.5$.

Figure 9 reveals the impact on the temperature profile of the thermophoresis parameter Nt . The limitations on thermophoresis helps in the increase of a surface temperature. The irregularity in motion (Brownian motion) causes a temperature increase due to the kinetic energy produced by nano-suspended particles; consequently, a thermophoretic force is produced. The fluid starts in the opposite direction of the stretching sheet, due to the intensity produced by this force. As a result, larger values of Nt cause an increase in temperature, due to which the surface temperature also increases.

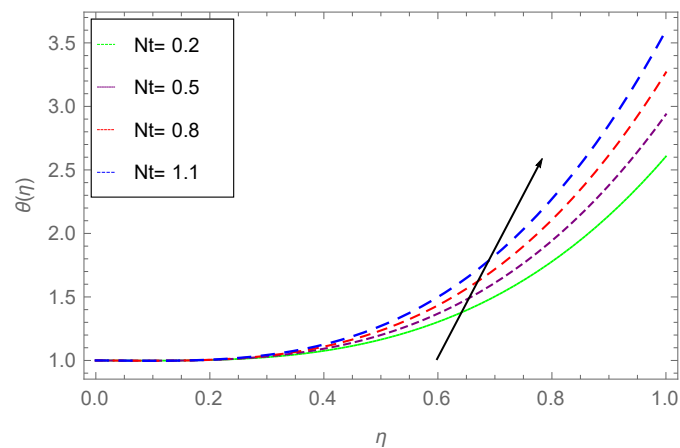


Figure 9. Impact of Nt on $\theta(\eta)$, for $\beta = 0.1$, $St = 0.1$, $Rd = 0.2$, $Nb = 0.3$.

Figure 10 demonstrates the effect on the profile of a heat $\theta(\eta)$ of the unsteadiness parameter St . It is observed that $\theta(\eta)$ directly varies with unsteadiness parameter St . The higher numbers of the unsteadiness parameter St increases the temperature, which further causes increase in the kinetic energy of the fluid, the result of which appears in the form of increase in the liquid film.

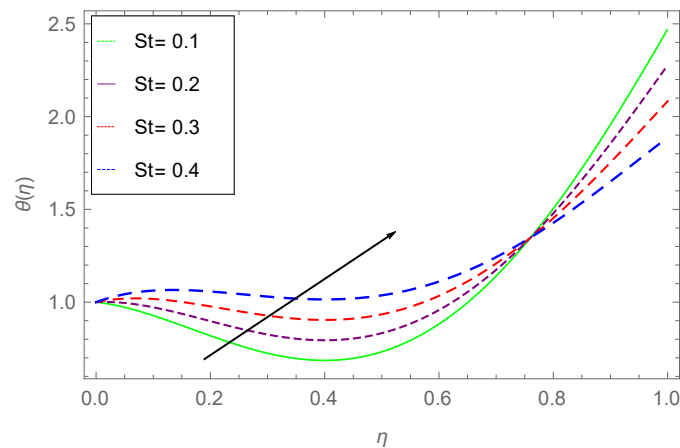


Figure 10. Impact of St on $\theta(\eta)$, for $\beta = 0.1$, $Nt = 0.8$, $Rd = 0.2$, $Nb = 0.5$.

The impact of thin film thickness β on temperature for different values of the embedded parameter is presented in Figure 11. Since the thickness parameter is the function of the kinematic viscosity and fluid thickness, so an increase in β would increase the viscosity, which further causes the decline of the temperature profile. Thus, for larger values of β , the profile of the temperature falls. The same effect can be seen in the profile of the velocity for β .

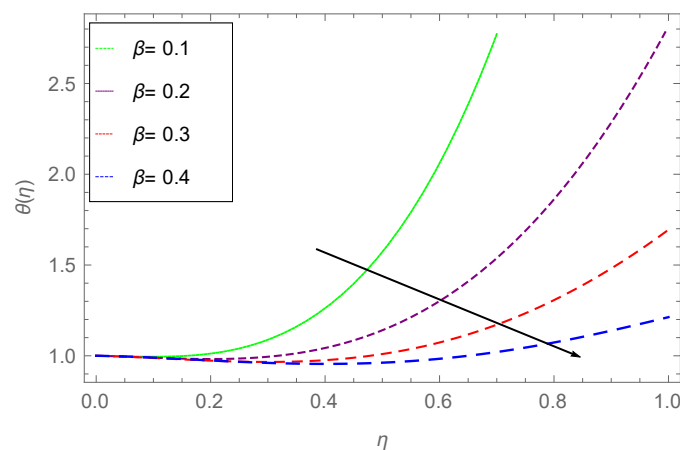


Figure 11. Impact of β on $\theta(\eta)$, for $St = 0.1$, $Nt = 0.5$, $Rd = 0.6$, $Nb = 0.5$.

Figure 12 illustrates the temperature distribution under Brownian motion parameter Nb . In general, due to the irregular motion of particles, a collision is produced between the particles. The figure shows that an increase in heat of the fluid can be observed with the ascending order of the Brownian motion parameter, Nb ; consequently, free surface nanoparticle volume friction decreases.

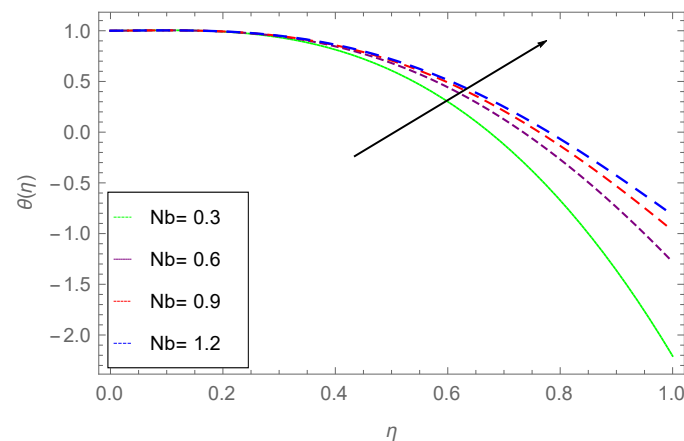


Figure 12. Impact of Nb on $\theta(\eta)$, for $St = 0.2$, $Nt = 0.6$, $Rd = 0.2$, $\beta = 0.1$.

7.3. Concentration Profile

Figure 13 illustrates the effects on concentration profile $\phi(\eta)$ of the Brownian motion parameter Nb . The irregularity and turbulence in the motion of the fluid particles is normally known as Brownian motion. At molecular level, Brownian motion of micropolar nanofluid leads to the thermal conductivity of nanofluids. The figure illustrates the increase in Nb in the form of a decline in the profile of the concentration. The boundary-layer thicknesses diminish due to the larger values of Brownian motion, which results in reduction of the concentration profile.

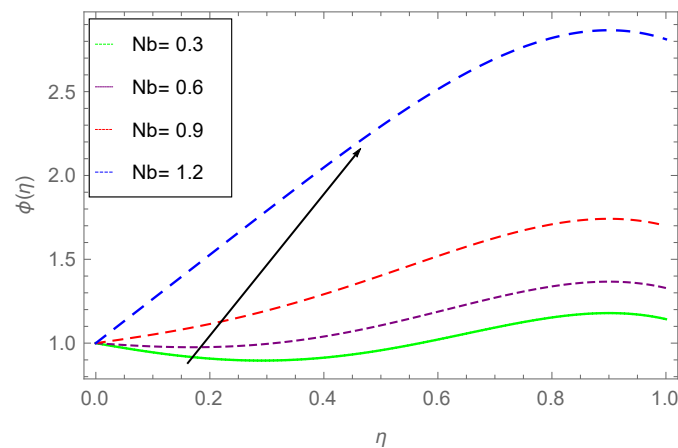


Figure 13. Impact of Nb on $\phi(\eta)$, for $St = 0.1$, $Nt = 0.1$, $Sc = 0.5$, and $\beta = 0.5$.

Figure 14 shows the concentration profile $\phi(\eta)$ behavior, under the effect of the unsteadiness parameter St . A direct relation can be observed between the unsteadiness parameter St and the concentration profile $\phi(\eta)$. Higher values of the unsteadiness parameter St increases the profile of temperature that blows the kinetic energy of the fluid, which further causes an increase in the concentration of the liquid film.

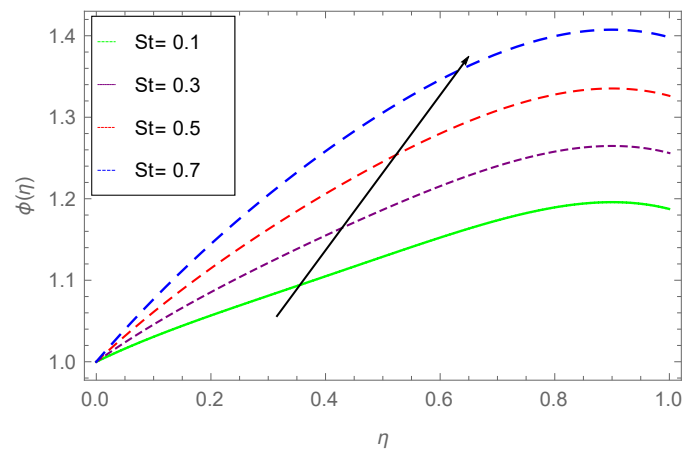


Figure 14. Impact of St on $\phi(\eta)$, for $Nt = 0.1$, $Nb = 1.2$, $Sc = 0.5$, and $\beta = 0.9$.

Figure 15 illustrates the effect on concentration field of the thermophoresis parameter Nt . The figure demonstrates that the concentration profile rises due to an increase in Nt . This is because of higher values of Nt increase the nanofluid molecule kinetic energy, as a result of which the concentration increases.

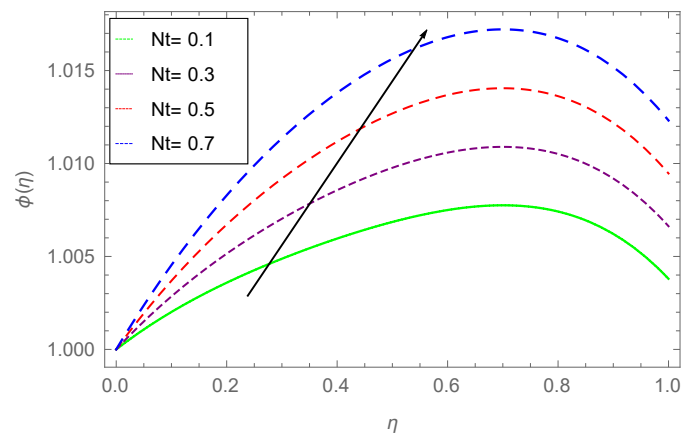


Figure 15. Impact of Nt on $\phi(\eta)$, when $St = 0.1$, $Sc = 0.5$, $Nb = 1.2$, $\beta = 0.9$.

Figure 16 illustrates the thin film thickness β effect on $\phi(\eta)$ for different values of the embedded parameters. The thickness parameter is inversely related to the kinematic viscosity; we know that kinematic viscosity is inversely proportional to the density of the fluid, so increasing the thickness parameter β causes the decline of the concentration profile. Thus, it is obvious that the concentration profile falls with higher numbers of β . The same effect was observed for β in the velocity distribution as well as in temperature distribution.

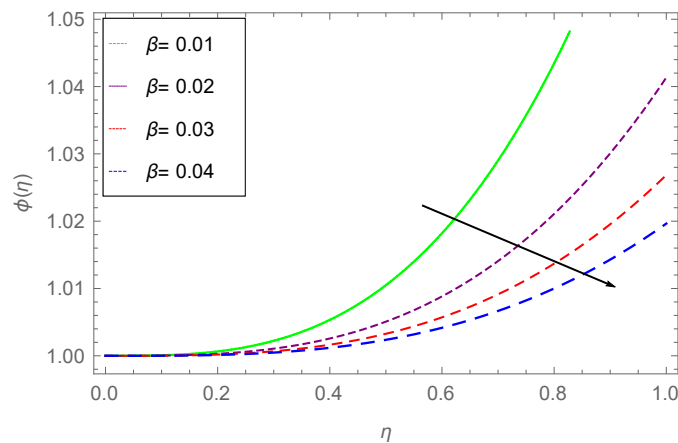


Figure 16. Impact of β on $\phi(\eta)$, when $Nt = 0.1$, $Nb = 0.3$, $Sc = 0.3$, $St = 0.1$.

Figure 17 demonstrates the opposite information as discussed in the temperature distribution under different parameters. The diagram shows that with increasing values of Schmidt number Sc , the concentration profile decreases, consequently reducing the thickness of the boundary-layer.

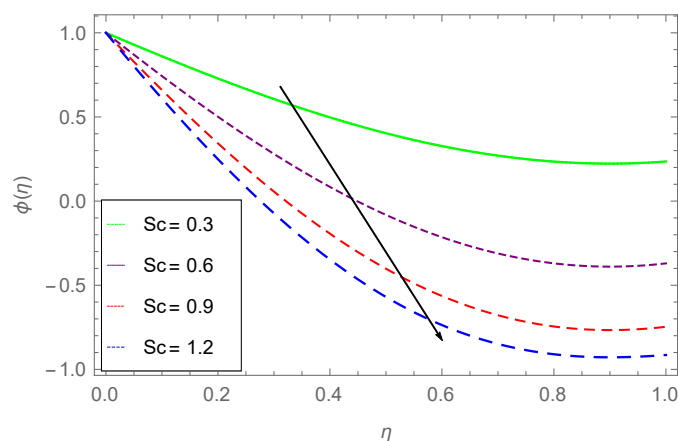


Figure 17. Impact of Sc on $\phi(\eta)$, for $Nt = 0.1$, $Nb = 0.3$, $\beta = 0.9$, $St = 0.1$.

7.4. Entropy Profile

The diagram reflects the variations of Brinkman number Br versus Bejan number B_e . It is observed that with increasing values of Br the Bejan number B_e declines. There is no variation in the Bejan number, and it remains constant up to 0.8 for the values of η in decreasing order for different values of the Brinkman number. Large variations are observed for smaller values of η as we increase the values of Brinkman number.

Figure 18 illustrates the variations in Bejan number under dissimilar values of the magnetic parameter M . It is clear from the figure that for larger values of M , the Bejan number boots up. Similar variations are observed for Brinkman number in Figure 19. The variations here are constant for smaller values of the magnetic parameter in the range of $0.85 < \eta \leq 1.0$. Large variations are investigated for greater values of the magnetic parameter in the range of $0.0 < \eta \leq 0.2$.

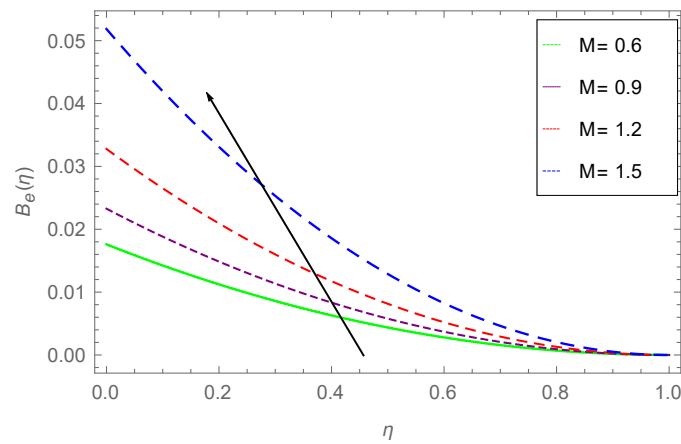


Figure 18. Deviations in Bejan number B_e for dissimilar numbers of M , when $Br = 0.1$, $R_e = 0.7$, $Rd = 0.6$, and $Pr = 0.6$.

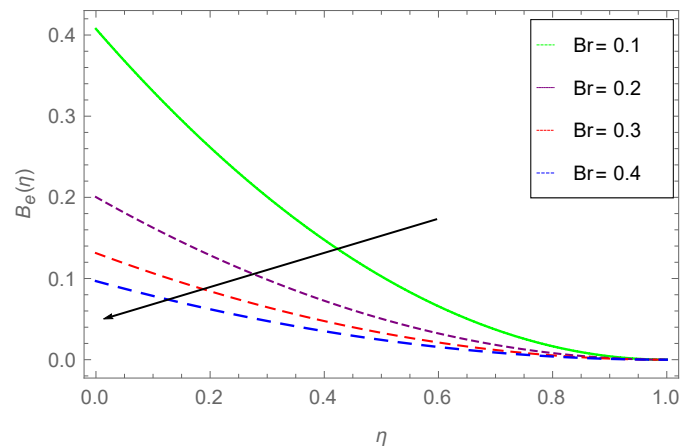


Figure 19. Variations in B_e for dissimilar values of Br , when $M = 0.1$, $R_e = 0.7$, $Rd = 0.6$, and $Pr = 0.6$.

Figure 20 illustrates the effect of Reynolds number on $N_G(\eta)$. For greater values of R_e the entropy regime increases. Consequently, Reynolds number and entropy function variates directly. From the graph it is clear that for large values of η the variations in entropy remains constant, while this variation jumps up for large values of the Reynolds number in the range of $0.0 \leq \eta \leq 0.4$.

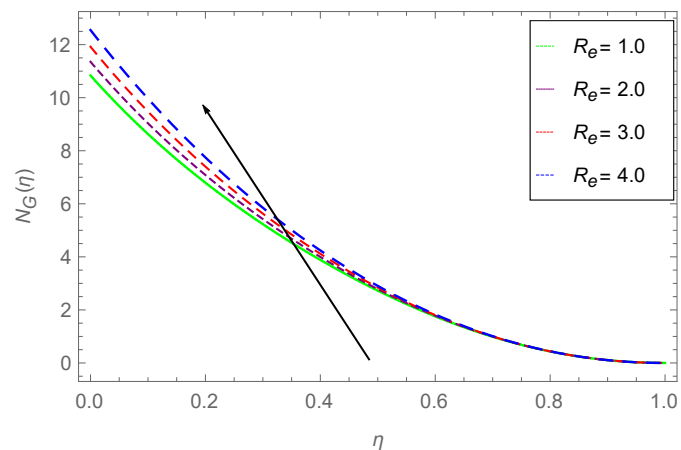


Figure 20. Variations in the function of entropy $N_G(\eta)$ for dissimilar values of R_e , when $Br = 0.1$, $Rd = 0.6$, $M = 1.3$.

Figure 21 demonstrates the variations in entropy number with the variations in Prandtl number Pr . The figure demonstrates that for larger values of the Prandtl number Pr , the temperature profile rises, and consequently, the entropy function boots up. The variations in the entropy function jumps up throughout inside the interval $0.0 \leq \eta \leq 1.0$. The increasing values of the Prandtl number increases the entropy function exponentially.

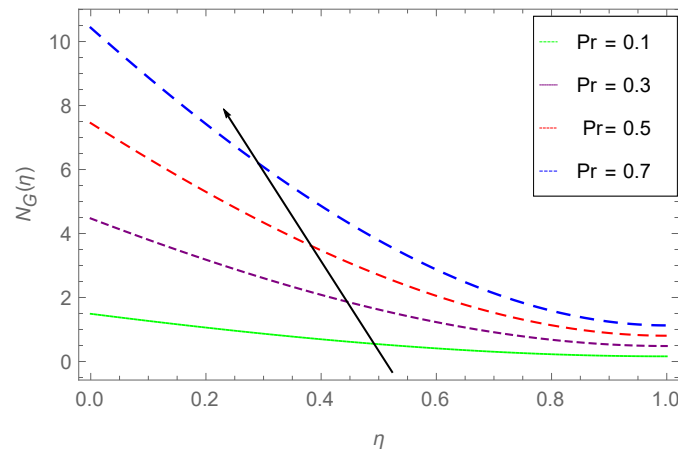


Figure 21. Variations in the function of entropy $N_G(\eta)$ for unlike values of Pr , when $Br = 0.3$, $R_e = 0.7$, $Rd = 0.7$ and $M = 0.9$.

Figure 22 demonstrates the variations of magnetic parameter on the entropy function $N_G(\eta)$. It is clear from the figure that for larger numbers of M , the entropy function reduces, because the Lorentz force in the magnetic field produces the resistance strength. These variations in the entropy function exist in the range of $0.0 \leq \eta \leq 0.65$ for larger values of the magnetic parameter, and remains constant elsewhere.

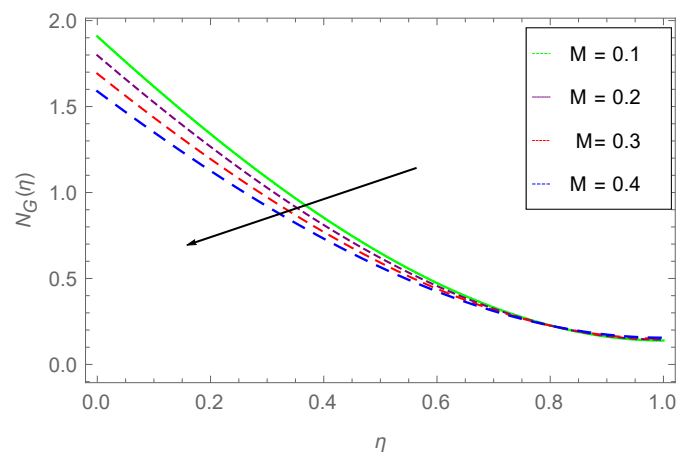


Figure 22. Variations in the function of entropy $N_G(\eta)$ for unlike values of M , when $Br = 0.3$, $R_e = 0.7$, $Rd = 0.7$ and $Pr = 1.2$.

Figure 23 demonstrates the effect of Brinkman number Br on the generation function of entropy generation $N_G(\eta)$. Figure shows that for larger numbers of the Brinkman number $N_G(\eta)$ increases. Viscous dissipation produces heat, which as a result raises the generation of entropy due to the lower conduction rate. The figure demonstrates that the variation in the entropy function remains constant between $0.64 < \eta \leq 1.0$, while an increasing tendency is observed for large values of the Brinkman number elsewhere.

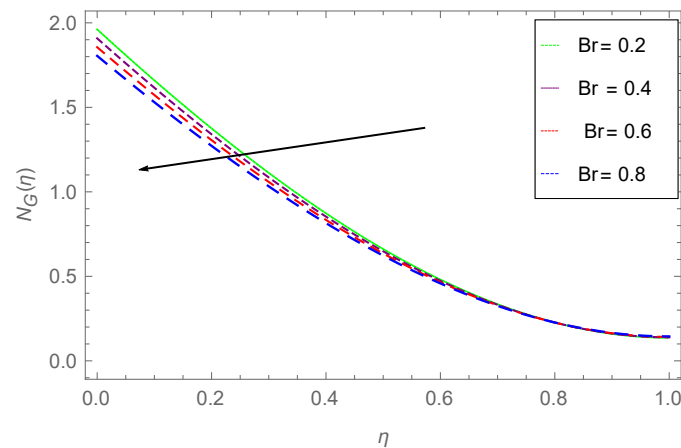


Figure 23. Variations in the function of entropy $N_G(\eta)$ for unlike values of Br , when $M = 0.7$, $R_e = 0.6$, $Rd = 0.8$ and $Pr = 1.5$.

7.5. Table Discussion

The influence of different parameters is demonstrated in Tables 2–4. Table 2 explains the effect on skin friction of M , Gr , β , and St . The skin-friction coefficient shows a rapid increase, with larger numbers of the unsteady parameter St , while for large values of the magnetic parameter M the Nusselt number decreases. On the other hand, larger values of the Grashof number Gr and thickness parameter β cause the decline of the skin-friction coefficient. Physically, Grashof number arises in the natural convection due to density difference. Viscous forces are also the functions of dependence of the Grashof number. Increasing the viscosity coefficient causes a decrease in the Grashof number. Therefore, as a result, the increasing values reduce the skin friction.

Table 3 reveals the effect on Nu of the parameters M , St , β , and Pr . It is noted that the larger the values of M (magnetic parameter), and the unsteadiness parameter St , the smaller the Nusselt number Nu . On the other hand, the Nusselt number Nu increases with larger values of unsteadiness parameter St and thickness parameter β . The increasing values of the Prandtl number decreases Nu .

The effects of Brownian motion Nb , thermophoretic parameter Nt , Schmidt number Sc , Prandtl Pr , and unsteadiness parameter St on Sherwood number are demonstrated in Table 4. It is clear that the increasing values of the thermophoretic parameter increases the Sherwood number. An inverse relation is observed between the Schmidt number and Sherwood number. The same phenomenon appears in observations for the unsteady parameter St and Prandtl number Pr for the Sherwood number in the form of decline. The larger values of the Prandtl number show an exponential decline in the Sherwood number.

Table 2. Variation in skin-friction coefficient, under dissimilar values of M , Gr , β and St .

M	Gr	β	St	C_f
0.1	0.5	0.1	1.5	−0.1708
0.5				−0.2034
1.0				−0.2460
1.5	0.1			−0.1776
	0.5			−0.1708
	1.0			−0.1708
	1.5	0.1		0.3434
		0.5		0.7463
		1.0		−6.9860
		1.5	0.1	−1.8672
			0.5	−0.2217
			1.0	−0.1320

Table 3. For dissimilar values of Pr , M , Rd and St variations in Nu (Nusselt Number).

M	β	St	Pr	Nu
0.1	0.1	1.5	1.5	0.3523
0.5				0.3521
1.0				0.3519
1.5	0.1			0.3523
	0.5			1.5145
	1.0			2.2616
	1.5	0.1		1.6248
		0.5		0.2284
		1.0		0.2904
		1.5	1.5	0.3523
			3.0	0.3243
			5.0	0.3087
			7.0	0.3012

Table 4. For dissimilar values of Nb , Nt , Sc , Pr , and St , variations in Sherwood Number.

Nb	Nt	Sc	St	Pr	Sh
0.1	0.5	0.1	1.5	1.5	-1.3582
0.5					-0.2388
1.0					-0.0988
1.5	0.1				0.0223
	0.5				-1.3582
	1.0				-2.7537
	1.5	0.1			-4.1455
		0.5			-3.9667
		1.0			-3.7453
		1.5	0.1		-1.8105
			0.5		-2.3059
			1.0		-2.9193
			1.5	1.5	-3.5263
				3.0	-5.6130
				5.0	-6.7706
				7.0	-7.3323

8. Conclusions

These reconsideration efforts are worthy enough to categorize the enhancement in heat transfer and thermal conductivity of non-Newtonian fluid with nanoparticle conductive properties. The velocity profile shows an increase with increasing value of the unsteadiness parameter St , while the increasing values of the magnetic parameter causes the decline of the velocity profile of the nanofluid film. It is shown that the coefficient of skin friction rises with the larger rates of the magnetic parameter M and the unsteadiness parameter St ; on the other hand, the coefficient of skin friction decreases with higher values of the stretching and thickness parameters. The temperature profile shows a direct variation with Brownian motion parameter. The thermal boundary-layer thickness decreases with increasing values of the of Sc . Nusselt number with increasing values of the radiation parameter increases. The surface temperature of the fluid increases with increasing values of Prandtl number, while an opposite tendency is observed with larger values of the unsteady parameter on the temperature profile. Similar results are investigated for the temperature profile with the variation of the thermophoresis parameter. The mass flux shows a decline with higher numbers of the Brownian motion parameter, while an opposite trend is experienced for the thermophoretic parameter. The implemented technique convergence is shown numerically for the validation of our technique.

Author Contributions: A.U., Z.S. and S.I. modeled the problem and wrote the manuscript. P.K. and M.A. thoroughly checked the mathematical modeling and English corrections. M.J. and A.U. solved the problem using

Mathematica software, and P.K., Z.S., M.J., and M.A. contributed to the results and discussions. All authors finalized the manuscript after its internal evaluation.

Funding: This research was funded by the Center of Excellence in Theoretical and Computational Science (TaCS-CoE), KMUTT.

Acknowledgments: This project was supported by the Theoretical and Computational Science (TaCS) Center under Computational and Applied Science for Smart Innovation Research Cluster (CLASSIC), Faculty of Science, KMUTT.

Conflicts of Interest: The authors declare no conflict of interest.

Abbreviations

The following abbreviations and parameters with their possible dimensions stated here are used in this article:

Sh	Sherwood number
β	Film thickness parameter
Nu	Nusselt number
St	Unsteady parameter
Re	Reynolds number
Pr	Prandtl number
ζ	Stretching parameter
Sc	Schmidt number
U_w	Stretching velocity ($\frac{m}{sec}$)
Nt	Thermophoretic parameter
C_f	Skin-friction coefficient
Nb	Brownian motion parameter
T	Cauchy stress tensor
T	Fluid temperature (K)
I	Identity tensor
ν	Kinematic viscosity ($\frac{m^2}{sec}$)
ρ	Density ($\frac{Kg}{m^3}$)
μ	Dynamic viscosity mPa
c_p	Specific heat ($\frac{J}{KgK}$)
$h(t)$	Thickness of liquid
Q_w	Heat Flux ($\frac{W}{m^2}$)
J_w	Mass flux ($\frac{Kg}{sec.m^2}$)
f	Dimensionless velocity
∞	Condition at infinity
0	Reference condition
\tilde{u}	Velocity component in x -direction ($\frac{m}{sec}$)
\tilde{v}	Velocity component in y -direction ($\frac{m}{sec}$)
x, y, z	Coordinates (m)
η	Similarity variable
t	Time (sec)
ω	Frequency parameter
$A_1, \text{ and } A_2$	Revinlin Erickson Tensor
E	Electric Field
α	Non-Newtonian Parameter
u_0	Magnetic Permeability
$\alpha_1 \text{ and } \alpha_2$	Material constants
Gm	Mixing parameter
σ	Electric conductivity
J	Current density

References

1. Myers, T. Application of non-Newtonian models to thin film flow. *Phys. Rev. E* **2005**, *72*, 066302. [[CrossRef](#)] [[PubMed](#)]
2. Marinca, V.; Herişanu, N.; Nemeş, I. Optimal homotopy asymptotic method with application to thin film flow. *Open Phys.* **2008**, *6*, 648–653. [[CrossRef](#)]
3. Sandeep, N.; Malvandi, A. Enhanced heat transfer in liquid thin film flow of non-Newtonian nanofluids embedded with graphene nanoparticles. *Adv. Powder Technol.* **2016**, *27*, 2448–2456. [[CrossRef](#)]
4. Wang, C. Liquid film on an unsteady stretching surface. *Q. Appl. Math.* **1990**, *48*, 601–610.
5. Usha, R.; Sridharan, R. On the motion of a liquid film on an unsteady stretching surface. *ASME Fluids Eng.* **1993**, *150*, 43–48. [[CrossRef](#)]
6. Liu, I.C.; Andersson, H.I. Heat transfer in a liquid film on an unsteady stretching sheet. *Int. J. Therm. Sci.* **2008**, *47*, 766–772. [[CrossRef](#)]
7. Aziz, R.C.; Hashim, I.; Alomari, A. Thin film flow and heat transfer on an unsteady stretching sheet with internal heating. *Meccanica* **2011**, *46*, 349–357. [[CrossRef](#)]
8. Tawade, L.; Abel, M.; Metri, P.G.; Koti, A. Thin film flow and heat transfer over an unsteady stretching sheet with thermal radiation, internal heating in presence of external magnetic field. *Int. J. Adv. Appl. Math. Mech.* **2016**, *3*, e40.
9. Andersson, H.I.; Aarseth, J.B.; Dandapat, B.S. Heat transfer in a liquid film on an unsteady stretching surface. *Int. J. Heat Mass Transf.* **2000**, *43*, 69–74. [[CrossRef](#)]
10. Chen, C.H. Heat transfer in a power-law fluid film over a unsteady stretching sheet. *Heat Mass Transf.* **2003**, *39*, 791–796. [[CrossRef](#)]
11. Chen, C.H. Effect of viscous dissipation on heat transfer in a non-Newtonian liquid film over an unsteady stretching sheet. *J. Non-Newton. Fluid Mech.* **2006**, *135*, 128–135. [[CrossRef](#)]
12. Ishaq, M.; Ali, G.; Shah, S.I.A.; Shah, Z.; Muhammad, S.; Hussain, S.A. Nanofluid Film Flow of Eyring Powell Fluid with Magneto Hydrodynamic Effect on Unsteady Porous Stretching Sheet. *J. Math.* **2019**, *51*, 131–153.
13. Shah, Z.; Bonyah, E.; Islam, S.; Gul, T. Impact of thermal radiation on electrical MHD rotating flow of Carbon nanotubes over a stretching sheet. *AIP Adv.* **2019**, *9*, 015115. [[CrossRef](#)]
14. Khan, A.; Nie, Y.; Shah, Z.; Dawar, A.; Khan, W.; Islam, S. Three-dimensional nanofluid flow with heat and mass transfer analysis over a linear stretching surface with convective boundary conditions. *Appl. Sci.* **2018**, *8*, 2244. [[CrossRef](#)]
15. Shah, Z.; Bonyah, E.; Islam, S.; Khan, W.; Ishaq, M. Radiative MHD thin film flow of Williamson fluid over an unsteady permeable stretching sheet. *Heliyon* **2018**, *4*, e00825. [[CrossRef](#)]
16. Megahed, A. Effect of slip velocity on Casson thin film flow and heat transfer due to unsteady stretching sheet in presence of variable heat flux and viscous dissipation. *Appl. Math. Mech.* **2015**, *36*, 1273–1284. [[CrossRef](#)]
17. Shah, Z.; Islam, S.; Ayaz, H.; Khan, S. Radiative heat and mass transfer analysis of micropolar nanofluid flow of Casson fluid between two rotating parallel plates with effects of Hall current. *J. Heat Transf.* **2019**, *141*, 022401. [[CrossRef](#)]
18. Jawad, M.; Shah, Z.; Islam, S.; Bonyah, E.; Khan, A.Z. Darcy-Forchheimer flow of MHD nanofluid thin film flow with Joule dissipation and Navier's partial slip. *J. Phys. Commun.* **2018**, *2*, 115014. [[CrossRef](#)]
19. Shah, Z.; Islam, S.; Gul, T.; Bonyah, E.; Khan, M.A. The electrical MHD and hall current impact on micropolar nanofluid flow between rotating parallel plates. *Results Phys.* **2018**, *9*, 1201–1214. [[CrossRef](#)]
20. Khan, A.; Shah, Z.; Islam, S.; Khan, S.; Khan, W.; Khan, A.Z. Darcy-Forchheimer flow of micropolar nanofluid between two plates in the rotating frame with non-uniform heat generation/absorption. *Adv. Mech. Eng.* **2018**, *10*, 1–16. [[CrossRef](#)]
21. Khan, A.; Shah, Z.; Islam, S.; Dawar, A.; Bonyah, E.; Ullah, H.; Khan, A. Darcy-Forchheimer flow of MHD CNTs nanofluid radiative thermal behaviour and convective non uniform heat source/sink in the rotating frame with microstructure and inertial characteristics. *AIP Adv.* **2018**, *8*, 125024. [[CrossRef](#)]
22. Shah, Z.; Dawar, A.; Islam, S.; Khan, I.; Ching, D.L.C. Darcy-Forchheimer flow of radiative carbon nanotubes with microstructure and inertial characteristics in the rotating frame. *Case Stud. Therm. Eng.* **2018**, *12*, 823–832. [[CrossRef](#)]

23. Khan, N.S.; Gul, T.; Islam, S.; Khan, A.; Shah, Z. Brownian motion and thermophoresis effects on MHD mixed convective thin film second-grade nanofluid flow with Hall effect and heat transfer past a stretching sheet. *J. Nanofluids* **2017**, *6*, 812–829. [[CrossRef](#)]
24. Tahir, F.; Gul, T.; Islam, S.; Shah, Z.; Khan, A.; Khan, W.; Ali, L. Flow of a nano-liquid film of Maxwell fluid with thermal radiation and magneto hydrodynamic properties on an unstable stretching sheet. *J. Nanofluids* **2017**, *6*, 1021–1030. [[CrossRef](#)]
25. Chu, R.C.; Simons, R. Recent development of computer cooling technology. In Proceedings of the International Symposium on Transport Phenomena in Thermal Engineering, Seoul, Korea, 9–13 May 1993; pp. 17–25.
26. Dixit, T.; Ghosh, I. Review of micro-and mini-channel heat sinks and heat exchangers for single phase fluids. *Renew. Sustain. Energy Rev.* **2015**, *41*, 1298–1311. [[CrossRef](#)]
27. Xie, X.; Liu, Z.; He, Y.; Tao, W. Numerical study of laminar heat transfer and pressure drop characteristics in a water-cooled minichannel heat sink. *Appl. Therm. Eng.* **2009**, *29*, 64–74. [[CrossRef](#)]
28. Srivastava, L.; Srivastava, V.; Sinha, S. Peristaltic transport of a physiological fluid. *Biorheology* **1983**, *20*, 153–166. [[CrossRef](#)]
29. Abbasi, F.M.; Hayat, T.; Shehzad, S.A.; Alsaadi, F.; Altoaibi, N. Hydromagnetic peristaltic transport of copper–water nanofluid with temperature-dependent effective viscosity. *Particuology* **2016**, *27*, 133–140. [[CrossRef](#)]
30. Abolbashari, M.H.; Freidoonimehr, N.; Nazari, F.; Rashidi, M.M. Analytical modeling of entropy generation for Casson nano-fluid flow induced by a stretching surface. *Adv. Powder Technol.* **2015**, *26*, 542–552. [[CrossRef](#)]
31. Hayat, T.; Muhammad, T.; Shehzad, S.; Alsaedi, A. Three-dimensional boundary layer flow of Maxwell nanofluid: mathematical model. *Appl. Math. Mech.* **2015**, *36*, 747–762. [[CrossRef](#)]
32. Malik, M.; Khan, I.; Hussain, A.; Salahuddin, T. Mixed convection flow of MHD Eyring-Powell nanofluid over a stretching sheet: A numerical study. *AIP Adv.* **2015**, *5*, 117118. [[CrossRef](#)]
33. Nadeem, S.; Haq, R.U.; Khan, Z. Numerical study of MHD boundary layer flow of a Maxwell fluid past a stretching sheet in the presence of nanoparticles. *J. Taiwan Inst. Chem. Eng.* **2014**, *45*, 121–126. [[CrossRef](#)]
34. Raju, C.; Sandeep, N.; Malvandi, A. Free convective heat and mass transfer of MHD non-Newtonian nanofluids over a cone in the presence of non-uniform heat source/sink. *J. Mol. Liq.* **2016**, *221*, 108–115. [[CrossRef](#)]
35. Rokni, H.B.; Alsaad, D.M.; Valipour, P. Electrohydrodynamic nanofluid flow and heat transfer between two plates. *J. Mol. Liq.* **2016**, *216*, 583–589. [[CrossRef](#)]
36. Nadeem, S.; Haq, R.U.; Khan, Z. Numerical solution of non-Newtonian nanofluid flow over a stretching sheet. *Appl. Nanosci.* **2014**, *4*, 625–631. [[CrossRef](#)]
37. Shehzad, S.; Hayat, T.; Alsaedi, A. MHD flow of Jeffrey nanofluid with convective boundary conditions. *J. Braz. Soc. Mech. Sci. Eng.* **2015**, *37*, 873–883. [[CrossRef](#)]
38. Sheikholeslami, M.; Hatami, M.; Ganji, D. Nanofluid flow and heat transfer in a rotating system in the presence of a magnetic field. *J. Mol. Liq.* **2014**, *190*, 112–120. [[CrossRef](#)]
39. Sheikholeslami, M.; Shah, Z.; Shafee, A.; Khan, I.; Tlili, I. Uniform magnetic force impact on water based nanofluid thermal behavior in a porous enclosure with ellipse shaped obstacle. *Sci. Rep.* **2019**, *9*, 1196. [[CrossRef](#)]
40. Mahmoodi, M.; Kandelousi, S. Kerosene- alumina nanofluid flow and heat transfer for cooling application. *J. Cent. South Univ.* **2016**, *23*, 983–990. [[CrossRef](#)]
41. Shah, Z.; Gul, T.; Islam, S.; Khan, M.A.; Bonyah, E.; Hussain, F.; Mukhtar, S.; Ullah, M. Three dimensional third grade nanofluid flow in a rotating system between parallel plates with Brownian motion and thermophoresis effects. *Results Phys.* **2018**, *10*, 36–45. [[CrossRef](#)]
42. Shah, Z.; Gul, T.; Khan, A.; Ali, I.; Islam, S.; Husain, F. Effects of hall current on steady three dimensional non-newtonian nanofluid in a rotating frame with brownian motion and thermophoresis effects. *J. Eng. Technol.* **2017**, *6*, e296.
43. Shah, Z.; Dawar, A.; Kumam, P.; Khan, W.; Islam, S. Impact of Nonlinear Thermal Radiation on MHD Nanofluid Thin Film Flow over a Horizontally Rotating Disk. *Appl. Sci.* **2019**, *9*, 1533. [[CrossRef](#)]
44. Saeed, A.; Islam, S.; Dawar, A.; Shah, Z.; Kumam, P.; Khan, W. Influence of Cattaneo–Christov Heat Flux on MHD Jeffrey, Maxwell, and Oldroyd-B Nanofluids with Homogeneous-Heterogeneous Reaction. *Symmetry* **2019**, *11*, 439. [[CrossRef](#)]

45. Kumam, P.; Shah, Z.; Dawar, A.; Rasheed, H.U.; Islam, S. Entropy Generation in MHD Radiative Flow of CNTs Casson Nanofluid in Rotating Channels with Heat Source/Sink. *Math. Probl. Eng.* **2019**, 2019. [[CrossRef](#)]
46. Khan, A.S.; Nie, Y.; Shah, Z. Impact of Thermal Radiation and Heat Source/Sink on MHD Time-Dependent Thin-Film Flow of Oldroyd-B, Maxwell, and Jeffrey Fluids over a Stretching Surface. *Processes* **2019**, *7*, 191. [[CrossRef](#)]
47. Nasir, S.; Shah, Z.; Islam, S.; Khan, W.; Khan, S.N. Radiative flow of magneto hydrodynamics single-walled carbon nanotube over a convectively heated stretchable rotating disk with velocity slip effect. *Adv. Mech. Eng.* **2019**, *11*. [[CrossRef](#)]
48. Nasir, S.; Shah, Z.; Islam, S.; Khan, W.; Bonyah, E.; Ayaz, M.; Khan, A. Three dimensional Darcy-Forchheimer radiated flow of single and multiwall carbon nanotubes over a rotating stretchable disk with convective heat generation and absorption. *AIP Adv.* **2019**, *9*, 035031. [[CrossRef](#)]
49. Saeed, A.; Shah, Z.; Islam, S.; Jawad, M.; Ullah, A.; Gul, T.; Kumam, P. Three-Dimensional Casson Nanofluid Thin Film Flow over an Inclined Rotating Disk with the Impact of Heat Generation/Consumption and Thermal Radiation. *Coatings* **2019**, *9*, 248. [[CrossRef](#)]
50. Sheikholeslami, M.; Bhatti, M. Forced convection of nanofluid in presence of constant magnetic field considering shape effects of nanoparticles. *Int. J. Heat Mass Transf.* **2017**, *111*, 1039–1049. [[CrossRef](#)]
51. Monfared, M.; Shamsavar, A.; Bahrebar, M.R. Second law analysis of turbulent convection flow of boehmite alumina nanofluid inside a double-pipe heat exchanger considering various shapes for nanoparticle. *J. Therm. Anal. Calorim.* **2019**, *135*, 1521–1532. [[CrossRef](#)]
52. Sheikholeslami, M. CuO-water nanofluid flow due to magnetic field inside a porous media considering Brownian motion. *J. Mol. Liq.* **2018**, *249*, 921–929. [[CrossRef](#)]
53. Sheikholeslami, M.; Shamlooei, M.; Moradi, R. Fe₃O₄-Ethylene glycol nanofluid forced convection inside a porous enclosure in existence of Coulomb force. *J. Mol. Liq.* **2018**, *249*, 429–437. [[CrossRef](#)]
54. Munkhbayar, B.; Tanshen, M.R.; Jeoun, J.; Chung, H.; Jeong, H. Surfactant-free dispersion of silver nanoparticles into MWCNT-aqueous nanofluids prepared by one-step technique and their thermal characteristics. *Ceram. Int.* **2013**, *39*, 6415–6425. [[CrossRef](#)]
55. Esfe, M.H.; Wongwises, S.; Naderi, A.; Asadi, A.; Safaei, M.R.; Rostamian, H.; Dahari, M.; Karimipour, A. Thermal conductivity of Cu/TiO₂-water/EG hybrid nanofluid: Experimental data and modeling using artificial neural network and correlation. *Int. Commun. Heat Mass Transf.* **2015**, *66*, 100–104. [[CrossRef](#)]
56. Akhgar, A.; Toghraie, D. An experimental study on the stability and thermal conductivity of water-ethylene glycol/TiO₂-MWCNTs hybrid nanofluid: Developing a new correlation. *Powder Technol.* **2018**, *338*, 806–818. [[CrossRef](#)]
57. Keyvani, M.; Afrand, M.; Toghraie, D.; Reiszadeh, M. An experimental study on the thermal conductivity of cerium oxide/ethylene glycol nanofluid: Developing a new correlation. *J. Mol. Liq.* **2018**, *266*, 211–217. [[CrossRef](#)]
58. Ranjbarzadeh, R.; Meghdadi, A.H.; Hojaji, M. The analysis of experimental process of production, stabilizing and measurement of the thermal conductivity coefficient of water/graphene oxide as a cooling nanofluid in machining. *J. Mod. Process. Manuf. Prod.* **2016**, *5*, 43–53.
59. Carreau, P.; Kee, D.D.; Daroux, M. An analysis of the viscous behaviour of polymeric solutions. *Can. J. Chem. Eng.* **1979**, *57*, 135–140. [[CrossRef](#)]
60. Kefayati, G.R.; Tang, H. MHD thermosolutal natural convection and entropy generation of Carreau fluid in a heated enclosure with two inner circular cold cylinders, using LBM. *Int. J. Heat Mass Transf.* **2018**, *126*, 508–530. [[CrossRef](#)]
61. Olajuwon, B.I. Convection heat and mass transfer in a hydromagnetic Carreau fluid past a vertical porous plate in presence of thermal radiation and thermal diffusion. *Therm. Sci.* **2011**, *15*, S241–S252. [[CrossRef](#)]
62. Hayat, T.; Asad, S.; Mustafa, M.; Alsaedi, A. Boundary layer flow of Carreau fluid over a convectively heated stretching sheet. *Appl. Math. Comput.* **2014**, *246*, 12–22. [[CrossRef](#)]
63. Alsarraf, J.; Moradikazerouni, A.; Shamsavar, A.; Afrand, M.; Salehipour, H.; Tran, M.D. Hydrothermal analysis of turbulent boehmite alumina nanofluid flow with different nanoparticle shapes in a minichannel heat exchanger using two-phase mixture model. *Phys. A Stat. Mech. Its Appl.* **2019**, *520*, 275–288. [[CrossRef](#)]
64. Azari, A.; Kalbasi, M.; Rahimi, M. CFD and experimental investigation on the heat transfer characteristics of alumina nanofluids under the laminar flow regime. *Braz. J. Chem. Eng.* **2014**, *31*, 469–481. [[CrossRef](#)]

65. Munir, A.; Shahzad, A.; Khan, M. Convective flow of Sisko fluid over a bidirectional stretching surface. *PLoS ONE* **2015**, *10*, e0130342. [[CrossRef](#)] [[PubMed](#)]
66. Olanrewaju, P.; Adigun, A.; Fenwa, O.; Oke, A.; Funmi, A. Unsteady free convective flow of sisko fluid with radiative heat transfer past a flat plate moving through a binary mixture. *Therm. Energy Power Eng.* **2013**, *2*, 109–117.
67. Khan, M.; Munawar, S.; Abbasbandy, S. Steady flow and heat transfer of a Sisko fluid in annular pipe. *Int. J. Heat Mass Transf.* **2010**, *53*, 1290–1297. [[CrossRef](#)]
68. Khan, M.; Shahzad, A. On boundary layer flow of a Sisko fluid over a stretching sheet. *Quaest. Math.* **2013**, *36*, 137–151. [[CrossRef](#)]
69. Patel, M.; Patel, J.; Timol, M. Laminar boundary layer flow of Sisko fluid. *Appl. Appl. Math.* **2015**, *10*, 909–918.
70. Darji, R.; Timol, M. Similarity analysis for unsteady natural convective boundary layer flow of Sisko fluid. *Int. J. Adv. Appl. Math. Mech.* **2014**, *1*, 22–36.
71. Siddiqui, A.; Hameed, A.; Haroon, T.; Walait, A. Analytic solution for the drainage of Sisko fluid film down a vertical belt. *Appl. Appl. Math.* **2013**, *8*, 465–480.
72. Khan, M.; Abbas, Q.; Duru, K. Magnetohydrodynamic flow of a Sisko fluid in annular pipe: A numerical study. *Int. J. Numer. Methods Fluids* **2010**, *62*, 1169–1180. [[CrossRef](#)]
73. Sari, G.; Pakdemirli, M.; Hayat, T.; Aksoy, Y. Boundary layer equations and Lie group analysis of a Sisko fluid. *J. Appl. Math.* **2012**, *2012*. [[CrossRef](#)]
74. Khan, H.; Haneef, M.; Shah, Z.; Islam, S.; Khan, W.; Muhammad, S. The combined magneto hydrodynamic and electric field effect on an unsteady Maxwell nanofluid flow over a stretching surface under the influence of variable heat and thermal radiation. *Appl. Sci.* **2018**, *8*, 160. [[CrossRef](#)]
75. Moallemi, N.; Shafieenejad, I.; Novinzadeh, A. Exact solutions for flow of a Sisko fluid in pipe. *Bull. Iran. Math. Soc.* **2011**, *37*, 49–60.
76. Dawar, A.; Shah, Z.; Islam, S.; Idress, M.; Khan, W. Magnetohydrodynamic CNTs Casson Nanofluid and Radiative heat transfer in a Rotating Channels. *J. Phys. Res. Appl.* **2018**, *1*, 017–032.
77. Shah, Z.; Dawar, A.; Khan, I.; Islam, S.; Ching, D.L.C.; Khan, A.Z. Cattaneo-Christov model for electrical magnetite micropolar Casson ferrofluid over a stretching/shrinking sheet using effective thermal conductivity model. *Case Stud. Therm. Eng.* **2019**, *13*, 100352. [[CrossRef](#)]
78. Khan, N.S.; Zuhra, S.; Shah, Z.; Bonyah, E.; Khan, W.; Islam, S. Slip flow of Eyring-Powell nanoliquid film containing graphene nanoparticles. *AIP Adv.* **2018**, *8*, 115302. [[CrossRef](#)]
79. Khan, W.; Pop, I. Boundary-layer flow of a nanofluid past a stretching sheet. *Int. J. Heat Mass Transf.* **2010**, *53*, 2477–2483. [[CrossRef](#)]
80. Osiac, M. The electrical and structural properties of nitrogen Ge₁Sb₂Te₄ thin film. *Coatings* **2018**, *8*, 117. [[CrossRef](#)]
81. Bahgat Radwan, A.; Abdullah, A.; Mohamed, A.; Al-Maadeed, M. New electrospun polystyrene/Al₂O₃ nanocomposite superhydrophobic coatings; synthesis, characterization, and application. *Coatings* **2018**, *8*, 65. [[CrossRef](#)]
82. Chen, X.; Dai, W.; Wu, T.; Luo, W.; Yang, J.; Jiang, W.; Wang, L. Thin film thermoelectric materials: Classification, characterization, and potential for wearable applications. *Coatings* **2018**, *8*, 244. [[CrossRef](#)]
83. Yamamuro, H.; Hatsuta, N.; Wachi, M.; Takei, Y.; Takashiri, M. Combination of electrodeposition and transfer processes for flexible thin-film thermoelectric generators. *Coatings* **2018**, *8*, 22. [[CrossRef](#)]
84. Khan, Z.; Shah, R.; Islam, S.; Jan, H.; Jan, B.; Rasheed, H.U.; Khan, A. MHD Flow and Heat Transfer Analysis in the Wire Coating Process Using Elastic-Viscous. *Coatings* **2017**, *7*, 15. [[CrossRef](#)]
85. Ullah, A.; Alzahrani, E.; Shah, Z.; Ayaz, M.; Islam, S. Nanofluids thin film flow of Reiner-Philippoff fluid over an unstable stretching surface with Brownian motion and thermophoresis effects. *Coatings* **2019**, *9*, 21. [[CrossRef](#)]
86. Bejan, A. Second-law analysis in heat transfer and thermal design. In *Advances in Heat Transfer*; Elsevier: Amsterdam, The Netherlands, 1982; Volume 15, pp. 1–58.
87. Bejan, A. Entropy generation minimization: The new thermodynamics of finite-size devices and finite-time processes. *J. Appl. Phys.* **1996**, *79*, 1191–1218. [[CrossRef](#)]
88. Weigand, B.; Birkefeld, A. Similarity solutions of the entropy transport equation. *Int. J. Therm. Sci.* **2009**, *48*, 1863–1869. [[CrossRef](#)]

89. Makinde, O.D. Second law analysis for variable viscosity hydromagnetic boundary layer flow with thermal radiation and Newtonian heating. *Entropy* **2011**, *13*, 1446–1464. [[CrossRef](#)]
90. Hayat, T.; Khan, M.I.; Khan, T.A.; Khan, M.I.; Ahmad, S.; Alsaedi, A. Entropy generation in Darcy-Forchheimer bidirectional flow of water-based carbon nanotubes with convective boundary conditions. *J. Mol. Liq.* **2018**, *265*, 629–638. [[CrossRef](#)]
91. Makinde, O. Thermodynamic second law analysis for a gravity-driven variable viscosity liquid film along an inclined heated plate with convective cooling. *J. Mech. Sci. Technol.* **2010**, *24*, 899–908. [[CrossRef](#)]
92. Esmailpour, M.; Abdollahzadeh, M. Free convection and entropy generation of nanofluid inside an enclosure with different patterns of vertical wavy walls. *Int. J. Therm. Sci.* **2012**, *52*, 127–136. [[CrossRef](#)]
93. Dawar, A.; Shah, Z.; Khan, W.; Idrees, M.; Islam, S. Unsteady squeezing flow of magnetohydrodynamic carbon nanotube nanofluid in rotating channels with entropy generation and viscous dissipation. *Adv. Mech. Eng.* **2019**, *11*. [[CrossRef](#)]
94. Feroz, N.; Shah, Z.; Islam, S.; Alzahrani, E.O.; Khan, W. Entropy Generation of Carbon Nanotubes Flow in a Rotating Channel with Hall and Ion-Slip Effect Using Effective Thermal Conductivity Model. *Entropy* **2019**, *21*, 52. [[CrossRef](#)]
95. Alharbi, S.; Dawar, A.; Shah, Z.; Khan, W.; Idrees, M.; Islam, S.; Khan, I. Entropy Generation in MHD Eyring–Powell Fluid Flow over an Unsteady Oscillatory Porous Stretching Surface under the Impact of Thermal Radiation and Heat Source/Sink. *Appl. Sci.* **2018**, *8*, 2588. [[CrossRef](#)]
96. Liao, S.J. The Proposed Homotopy Analysis Technique for the Solution of Nonlinear Problems. Ph.D. Thesis, Shanghai Jiao Tong University, Shanghai, China, 1992.
97. Liao, S.J. An explicit, totally analytic approximate solution for Blasius' viscous flow problems. *Int. J. Non-Linear Mech.* **1999**, *34*, 759–778. [[CrossRef](#)]
98. Liao, S.J. On the analytic solution of magnetohydrodynamic flows of non-Newtonian fluids over a stretching sheet. *J. Fluid Mech.* **2003**, *488*, 189–212. [[CrossRef](#)]
99. Abbasbandy, S.; Jalili, M. Determination of optimal convergence-control parameter value in homotopy analysis method. *Numer. Algorithms* **2013**, *64*, 593–605. [[CrossRef](#)]



© 2019 by the authors. Licensee MDPI, Basel, Switzerland. This article is an open access article distributed under the terms and conditions of the Creative Commons Attribution (CC BY) license (<http://creativecommons.org/licenses/by/4.0/>).